

# Magnetic excitations in coupled Haldane spin chains near the quantum critical point

A. Zheludev

*Physics Department, Brookhaven National Laboratory, Upton, NY 11973-5000, USA.*

T. Masuda,<sup>\*</sup> I. Tsukada,<sup>†</sup> Y. Uchiyama,<sup>‡</sup> and K. Uchinokura,<sup>\*</sup>

*Department of Applied Physics, The University of Tokyo, 6th Engineering Bld., 7-3-1 Bunkyo-ku, Tokyo 113-8656, Japan.*

P. Böni

*Paul Scherrer Institut, 5232 Villigen PSI, Switzerland.*

S.-H. Lee

*NIST Center for Neutron Research, National Institute of Standards and Technology, MD 20899, USA.*

<sup>\*</sup> *Present address: also Department of Advanced Material Science, the University of Tokyo.*

<sup>†</sup> *Present address: Central Research Institute of Electric power Industry, 2-11-1, Iwato kita, Komae-shi, Tokyo 201-8511, Japan.*

<sup>‡</sup> *Present address: ULSI Device Development Laboratory, NEC Corporation.*

(February 6, 2008)

Two quasi-1-dimensional  $S = 1$  quantum antiferromagnetic materials,  $\text{PbNi}_2\text{V}_2\text{O}_8$  and  $\text{SrNi}_2\text{V}_2\text{O}_8$ , are studied by inelastic neutron scattering on powder samples. While magnetic interactions in the two systems are found to be very similar, subtle differences in inter-chain interaction strengths and magnetic anisotropy are detected. The latter are shown to be responsible for qualitatively different ground state properties: magnetic long-range order in  $\text{SrNi}_2\text{V}_2\text{O}_8$  and disordered “spin liquid” Haldane-gap state in  $\text{PbNi}_2\text{V}_2\text{O}_8$ .

## I. INTRODUCTION

After two decades of intensive theoretical and experimental studies, 1-dimensional (1D) Heisenberg quantum antiferromagnets (AF) are now rather well understood. A great deal of work has been done on integer-spin systems that have a spin-liquid ground state and a famous Haldane gap in the magnetic excitation spectrum.<sup>1,2</sup> The focus in quantum magnetism has now shifted towards studies of more complex phenomena, that include inter-chain interactions, spin-lattice coupling, and/or spin-vacancies and substitutions. Of particular current interest is the quantum phase transition between spin-liquid (non-magnetic) and ordered states. This type of transition in gapped 1D systems occurs as 3D magnetic interactions and/or magnetic anisotropy are increased beyond certain threshold values. Their effect is to lower the energy of excitations at certain points in reciprocal space, and ultimately induce to a soft-mode transition to a Néel-like ordered structure. An example of such behavior is found in the extensively studied  $\text{CsNiCl}_3$  compound.<sup>3-6</sup> The corresponding phase diagram has been worked out by several authors, including Sakai and Takahashi<sup>7</sup> (Fig. 1).

The most direct way to observe such a transition experimentally is by looking at a series of isostructural compounds with slightly different inter-chain coupling constants or anisotropy terms. The problem is that most known quasi-1D  $S = 1$  AF materials are otherwise deep inside the spin-liquid area of the phase diagram (good 1-D systems), or obviously in the 3D Néel-like or XY-like ordered phases (Fig. 1).  $\text{CsNiCl}_3$  and related compounds<sup>3,5,8</sup> are perhaps the only systems close to the phase boundary that have been extensively studied to date. Unfortunately, these compounds order in 3 dimensions at low temperature, and have no isostructural counterpart with a spin-liquid ground state. Only about a year ago the first quasi-1-D integer-spin AF that is still in the spin-liquid state, but is on the verge of a 3D ordering instability, was characterized.<sup>9</sup> This Haldane-gap material,  $\text{PbNi}_2\text{V}_2\text{O}_8$  is so close to the phase boundary that LRO, absent in the pure compound, can be induced by spin-vacancy substitution.<sup>9</sup> Moreover, an isostructural undoped system, namely  $\text{SrNi}_2\text{V}_2\text{O}_8$  *does* order in 3-dimensions at low temperatures. For the first time two very similar stoichiometric quasi-1D materials with such vastly different ground state properties can be compared in experimental studies.

The magnetic properties of both  $\text{PbNi}_2\text{V}_2\text{O}_8$  and  $\text{SrNi}_2\text{V}_2\text{O}_8$  are due to spin  $S = 1$  octahedrally-coordinated  $\text{Ni}^{2+}$  ions, while the  $\text{V}^{5+}$  sites are presumed to be non-magnetic. The crystal structure, visualized in Fig. 2a, is tetragonal, space group  $I41cd$ , with lattice constants  $a = 12.249(3)$  Å,  $c = 8.354(2)$  Å for  $\text{PbNi}_2\text{V}_2\text{O}_8$ ,<sup>10</sup> and

$a = 12.1617 \text{ \AA}$ ,  $c = 8.1617 \text{ \AA}$  for  $\text{SrNi}_2\text{V}_2\text{O}_8$ ,<sup>11</sup> respectively. The magnetic Ni-sites are arranged in peculiar spiral-shaped chains that run along the unique crystal axis, as shown in Fig. 2b. Even though all nearest neighbor Ni-Ni bonds are crystallographically equivalent, the spin-spirals have a step-4 periodicity. The dominant magnetic interaction is antiferromagnetic, between nearest-neighbor  $\text{Ni}^{2+}$  spins within each chain. The corresponding exchange constant,  $J \approx 8.2 \text{ meV}$  in both systems, was deduced from the high-temperature part of the experimental  $\chi(T)$  curves.<sup>9</sup> The ground state of  $\text{PbNi}_2\text{V}_2\text{O}_8$  is a Haldane singlet, and the excitation spectrum has an energy gap, as unambiguously shown in low-temperature  $\chi(T)$  and  $C(T)$  measurements. The energy gaps, 1.2 meV and 2.2 meV, for excitations polarized along, and perpendicular to the chain-axis, respectively, were accurately determined in high-field magnetization studies. The observed anisotropy of the spin gap is attributed to single-ion easy-axis magnetic anisotropy on the Ni-sites  $D \approx -0.23 \text{ meV}$ .

Unlike  $\text{PbNi}_2\text{V}_2\text{O}_8$ ,  $\text{SrNi}_2\text{V}_2\text{O}_8$  orders magnetically in three dimensions at  $T_N = 7 \text{ K}$ . The magnetic structure has not been determined to date, but, according to bulk measurements, is of a weak-ferromagnetic type, with a dominant antiferromagnetic component. The ordered staggered moment is along the unique  $c$  crystallographic axis. The weak-ferromagnet distortion of this Néel (collinear) spin arrangement is attributed to the presence of weak Dzyaloshinskii-Moriya off-diagonal exchange interactions in the non-centric crystal.

Preliminary inelastic neutron scattering studies<sup>9</sup> provided an estimate for the inter-chain interaction strength. Only a limited amount of neutron data are available for  $\text{PbNi}_2\text{V}_2\text{O}_8$ , and, to date, none for  $\text{SrNi}_2\text{V}_2\text{O}_8$ . The present paper deals with more extensive comparative inelastic neutron scattering studies of both materials. Our results reveal the subtle differences between the two systems, responsible for their vastly distinct ground state properties.

## II. MAGNETIC INTERACTIONS

Prior to reporting our new experimental findings, we shall briefly discuss the magnetic interactions that may play an important role in the physics of  $\text{PbNi}_2\text{V}_2\text{O}_8$  and  $\text{SrNi}_2\text{V}_2\text{O}_8$ , and construct a model spin Hamiltonian for these systems. In doing so, we shall introduce the notation used throughout the rest of the paper.

As mentioned in the introduction, all previous studies point to that the dominant magnetic interaction is the antiferromagnetic coupling  $J$  between nearest-neighbor spins ( $2.78 \text{ \AA}$ ) within each spiral-shaped chain. It is also clear that taking the expectedly weaker inter-chain interactions into account is crucial to understanding the static and dynamic properties. In our previous work (Ref. 9) we assumed that the dominant inter-chain coupling is between pairs of  $\text{Ni}^{2+}$  ions from adjacent chains, such that both interacting spins have the same  $c$ -axis fractional cell coordinate, and that each Ni-site is coupled to 4 other sites. The resulting coupling topology is schematized in Fig. 4a. Considering only these inter-chain bonds, however, can not result in a very realistic model. First of all, they do not correspond to the shortest inter-chain Ni-Ni distance. More importantly, in the crystal structure of  $\text{PbNi}_2\text{V}_2\text{O}_8$ , there seem to be no obvious superexchange pathways corresponding to these links. If one pays close attention to crystal symmetry, bond length, and possible superexchange routes involving the  $\text{VO}_4$  tetrahedra, one arrives at a more complex interaction geometry, visualized in Fig. 3. Here one assumes interactions along the shortest inter-chain Ni-Ni bond ( $5.0 \text{ \AA}$ ). Coupled  $\text{Ni}^{2+}$  ions are offset relative to each other by  $c/4$  along the chain axis, and are bridged by a  $\text{VO}_4$  tetrahedron. All such bonds are crystallographically equivalent. Each Ni-site is linked with only two adjacent chains. The overall coupling topology for this model is as shown in Fig. 4b. We shall denote the corresponding exchange constant as  $J_1$ .

Magnetic anisotropy is clearly manifest in bulk susceptibility and magnetization measurements, and must be explicitly included in the spin Hamiltonian. Because of the strong dispersion along the chain-axis, all the low-energy response of each chain is concentrated at wave vectors close to the 1-D AF zone-center. In this long-wavelength limit, 2-ion anisotropy of in-chain interactions and single-ion anisotropy associated with individual spins can not be distinguished. In our model we shall therefore include only the latter, and write the corresponding term in the Hamiltonian as:

$$\hat{H}_{\text{single-ion}} = D \sum_{i,k} (S_{i,k}^z)^2. \quad (1)$$

The choice of the anisotropy axis along the chain direction is based on previous bulk magnetic studies. Here  $D$  is the anisotropy constant ( $D < 0 = \text{easy-axis}$ ) and  $\mathbf{S}_{i,k}$  is the spin operator for site  $i$  in chain  $k$ . At the same time we shall assume in-chain exchange interactions to be isotropic and write this Heisenberg term as:

$$\hat{H}_{\text{in-chain}} = J \sum_{i,k} \mathbf{S}_{i,k} \mathbf{S}_{i+1,k}. \quad (2)$$

The magnitude of dispersion perpendicular to the chain axis is expected to be rather small, so the entire range of wave vector transfers in the  $(a, b)$  plane will influence the low-energy properties. For this reason, two-ion anisotropy of  $J_1$ ,

unlike that of  $J$ , is a relevant parameter and should be considered. The inter-chain coupling term in the Hamiltonian will thus have the form:

$$\hat{H}_{\text{inter-chain}} = \sum_{i,i',k,k'} \left[ J_{1,\parallel} S_{i,k}^z S_{i',k'}^z + J_{1,\perp} \left\{ S_{i,k}^x S_{i',k'}^x + S_{i,k}^y S_{i',k'}^y \right\} \right]. \quad (3)$$

Here the sum is taken over pairs of next-nearest-neighbor spins. The three terms discussed above constitute the spin Hamiltonian that we propose for  $\text{PbNi}_2\text{V}_2\text{O}_8$  and  $\text{SrNi}_2\text{V}_2\text{O}_8$ . Of course, other magnetic interactions can be active in the system as well. As will be discussed below, however, the described model can reproduce the experimental data with a minimal number of parameters.

### III. EXPERIMENTAL

Inelastic neutron scattering studies of  $\text{PbNi}_2\text{V}_2\text{O}_8$  and  $\text{SrNi}_2\text{V}_2\text{O}_8$  powder samples (about 10 g each) were carried out in two series of experiments. The conventional 3-axis technique was used to measure certain characteristic constant- $E$  and constant- $Q$  scans. These measurements were performed at the TASP and Druchal spectrometers at the continuous spallation source SINQ at Paul Scherrer Institute. Neutrons of a fixed final energy of 5 meV or 8 meV were used with pyrolytic graphite (PG) monochromator and analyzer, and a typical (open) – 80' – 80' – (open)' collimation setup. For some scans a horizontally focusing analyzer was used to increase the useful scattered intensity, in which case no collimators were used after the sample. In most of the measurements a flat analyzer was employed instead. In the 5 meV-final configuration a Be filter was inserted after the sample to suppress higher-order beam contamination. The spectrum of neutrons emerging from the guide is such that no higher-order filter was required for the 8 meV-final measurements.

In the second series of experiments we took advantage of the area-sensitive detector (ASD) 3-axis setup available for the NG-5 “SPINS” spectrometer installed at the National Institute of Standards and Technology. In special cases when a large domain of  $E - Q$  space needs to be surveyed in a spherically symmetric sample (such as powder) this technique can provide an amazing, almost 10-fold increase of data collection rate, as compared to the standard 3-axis geometry, without any penalty in resolution. In our experiments on  $\text{PbNi}_2\text{V}_2\text{O}_8$  and  $\text{SrNi}_2\text{V}_2\text{O}_8$  we utilized a PG monochromator and a (open) – 80' – 80' – 80' (radial) array of collimators. The measurements were done in the fixed-final-energy mode, with the central blade of the composite analyzer tuned to  $E_f = 3.125$  meV. In the experiment scattering events with final neutron energies in the range  $E_f \pm 0.4$  meV are registered simultaneously. To suppress higher-order beam contamination we used a Be-O filter after the sample. The data were taken for momentum and energy transfers of up to  $2.5 \text{ \AA}^{-1}$  and 7 meV, respectively.

In both series of experiments the sample environment was a standard “ILL-orange” cryostat, and the temperature range 1.5 – 30 K was covered. The background was measured by repeating some scans with the analyzer moved away from its elastic position by  $10^\circ$ . In the SPINS experiment the background due to air scattering was separately measured with the sample removed from the spectrometer.

### IV. EXPERIMENTAL RESULTS

#### A. Results obtained at low temperatures

The inelastic neutron scattering intensities measured in  $\text{PbNi}_2\text{V}_2\text{O}_8$  and  $\text{SrNi}_2\text{V}_2\text{O}_8$  at  $T = 1.2$  K with the ASD setup are shown in the false-color plot in Fig. 5 (background subtracted). The resolution of the area-sensitive detector is greater than the actual energy and wave vector resolution of the spectrometer (0.11 meV and  $0.023 \text{ \AA}^{-1}$  at  $\hbar\omega = 0$ ). The customary procedure is to re-bin the mesh data to a coarser grid. Instead, for visualization purposes, the data in Fig. 5 were smeared using a fixed-resolution  $0.5 \text{ meV} \times 0.06 \text{ \AA}^{-1}$  FWHM Gaussian filter. As reported previously,<sup>9</sup> constant-energy scans measured in  $\text{PbNi}_2\text{V}_2\text{O}_8$  at 4 meV energy transfer have a peculiar and very characteristic shape. Such scans were collected at  $T = 2$  K for both materials, using the 8 meV-final/flat analyzer setup SINQ. These scans are shown in Fig. 6. In addition, representative constant- $Q$  scans were also measured in this configuration, and are shown in Figs. 7 and 8.

Despite the different ground states, the main features of the powder-averaged dynamic cross section for the two materials are quite similar. This, however, is not particularly surprising. The dynamic structure factor  $S(\mathbf{Q}, \omega)$  is severely smeared out by the spherical averaging that occurs in a powder sample. The main features are defined by the form factor of each spiral-shaped chain, and by the steep dispersion along the chain axis, expected to be almost identical in the two systems. The significant difference between the two materials is expected to be in the magnitude

of the inter-chain interactions, and possibly single-ion anisotropy. These effects are much more difficult to observe, as they only influence the weak spin wave dispersion in the  $(a, b)$  crystallographic plane. Our data do in fact contain relevant information on the transverse dispersion of spin excitations, which can be extracted from a quantitative analysis, as described in the following section.

## B. Data analysis

### 1. Model cross section

The general problem in interpreting inelastic neutron scattering data from powder samples is an effective loss of information upon spherical averaging. Indeed, the quantity of interest is the dynamic structure factor  $S(\mathbf{Q}, \omega)$  that for each channel of spin polarization is a scalar function in 4-dimensional  $E - \mathbf{Q}$  space. In a powder sample one measures the spherical average of this function, a scalar function defined in 2-dimensional space:

$$S_{\text{powder}}(Q, \omega) = \frac{1}{4\pi} \int d\phi \sin \theta d\theta S([Q \sin \theta \cos \phi, Q \sin \theta \sin \phi, Q \cos \theta], \omega) \quad (4)$$

The transformation  $S(\mathbf{Q}, \omega) \rightarrow S_{\text{powder}}(Q, \omega)$  is not reversible. The only way the full correlation function can be extracted from the experiment is by assuming some parameterized model for  $S(\mathbf{q}, \omega)$  and fitting it to the measured  $S_{\text{powder}}(Q, \omega)$ . For  $\text{PbNi}_2\text{V}_2\text{O}_8$  and  $\text{SrNi}_2\text{V}_2\text{O}_8$  we used the following analytical form for  $S(\mathbf{q}, \omega)$ , as derived below in the theory section:

$$S(\mathbf{Q}) = P_{\parallel}(\mathbf{Q})S_{\parallel}(\mathbf{Q}) + P_{\perp}(\mathbf{Q})S_{\perp}(\mathbf{Q}), \quad (5)$$

$$\begin{aligned} 2S_{\parallel}(\mathbf{Q}) &= 2 \cos^2 \psi_1 \cos^2 \psi_2 S'_{\parallel}(h, k, l) \\ &\quad + \cos^2 \psi_1 \sin^2 \psi_2 [S'_{\parallel}(h+1, k, l+1) + S'_{\parallel}(h+1, k, l+3)] \\ &\quad + \sin^2 \psi_1 \cos^2 \psi_2 [S'_{\parallel}(h, k+1, l+1) + S'_{\parallel}(h, k+1, l+3)] \\ &\quad + 2 \sin^2 \psi_1 \sin^2 \psi_2 S'(h+1, k+1, l+2), \end{aligned} \quad (6)$$

$$\begin{aligned} 2S_{\perp}(\mathbf{Q}) &= 2 \cos^2 \psi_1 \cos^2 \psi_2 S'_{\perp}(h, k, l) \\ &\quad + \cos^2 \psi_1 \sin^2 \psi_2 [S'_{\perp}(h+1, k, l+1) + S'_{\perp}(h+1, k, l+3)] \\ &\quad + \sin^2 \psi_1 \cos^2 \psi_2 [S'_{\perp}(h, k+1, l+1) + S'_{\perp}(h, k+1, l+3)] \\ &\quad + 2 \sin^2 \psi_1 \sin^2 \psi_2 S'(h+1, k+1, l+2), \end{aligned} \quad (7)$$

$$\psi_1 = \frac{\pi d}{a} h, \quad (8)$$

$$\psi_2 = \frac{\pi d}{a} k. \quad (9)$$

In these formulas the argument  $\omega$  has been dropped. The phases  $\psi_1$  and  $\psi_2$  represent the 3-D structure factor of the spiral-shaped spin chains, and  $d = 0.08a$  is the offset of each  $\text{Ni}^{2+}$ -ion relative to the central axis of the corresponding spiral chain, along the  $a$  or  $b$  axis. The polarization factors for longitudinal (polarization along the  $c$ -axis) and transverse (polarization in the  $(a, b)$  plane) spin excitations are defined as:

$$P_{\parallel}(\mathbf{Q}) = \sin^2(\widehat{\mathbf{Q}}, \mathbf{z}), \quad (10)$$

$$P_{\perp}(\mathbf{Q}) = 1 + \cos^2(\widehat{\mathbf{Q}}, \mathbf{z}). \quad (11)$$

The dynamic structure factors  $S'_{\parallel}$  and  $S'_{\perp}$  for straight (as opposed to spiral-shaped) Haldane chains are written in the Single-Mode Approximation (SMA)<sup>12–14</sup>:

$$S'_{\parallel}(\mathbf{Q}, \omega) = \frac{Zv}{\hbar\omega_{\parallel}(\mathbf{Q})} \delta(\hbar\omega - \hbar\omega_{\parallel}(\mathbf{Q})), \quad (12)$$

$$S'_{\perp}(\mathbf{Q}, \omega) = \frac{Zv}{\hbar\omega_{\perp}(\mathbf{Q})} \delta(\hbar\omega - \hbar\omega_{\perp}(\mathbf{Q})). \quad (13)$$

Here  $v = 2.48J$  is the spin wave velocity, and  $Z = 1.26$  (Ref. 15). Finally, the dispersion relation for weakly coupled chains are given by:

$$[\hbar\omega_{\parallel}(\mathbf{Q})]^2 = \Delta_{\parallel}^2 + v^2 \sin^2(\pi l/2) - \frac{1}{2}ZvJ_{1,\parallel} \cos(\pi l/2) [\cos(\pi h) + \cos(\pi k)] (1 - \cos \pi l/2), \quad (14)$$

$$[\hbar\omega_{\perp}(\mathbf{Q})]^2 = \Delta_{\perp}^2 + v^2 \sin^2(\pi l/2) - \frac{1}{2}ZvJ_{1,\perp} \cos(\pi l/2) [\cos(\pi h) + \cos(\pi k)] (1 - \cos \pi l/2), \quad (15)$$

where  $\Delta_{\parallel}$  and  $\Delta_{\perp}$  are the longitudinal and transverse *intrinsic Haldane* gaps for non-interacting chains, respectively. The splitting of the triplet in our model is caused by single-ion anisotropy:<sup>16</sup>

$$\Delta_{\perp} = \langle \Delta \rangle - 0.57D, \quad (16)$$

$$\Delta_{\parallel} = \langle \Delta \rangle + 1.41D. \quad (17)$$

An important parameter is the *mean* intrinsic Haldane gap  $\langle \Delta \rangle \equiv (\Delta_{\parallel} + 2\Delta_{\perp})/3$ . As can be seen from Eqs. 16 and 17, it is, to the first order, defined by  $J$  alone:  $\langle \Delta \rangle \approx 0.41J$ .<sup>16</sup> It is also useful to define the actual gaps (excitation energies at the 3-D AF zone-center):

$$E_{\min,\perp}^2 = \Delta_{\perp}^2 - 2Zv|J_{1,\perp}|, \quad (18)$$

$$E_{\min,\parallel}^2 = \Delta_{\parallel}^2 - 2Zv|J_{1,\parallel}|. \quad (19)$$

The spherical average of Eq. 5 was calculated numerically using a Monte-Carlo algorithm that also eliminates the  $\delta$ -functions in Eqs. 12 and 13. The parameters were then refined by a standard least-squares routine to best-fit the data. To accelerate the fitting process the ASD data were binned to a rectangular  $0.046 \text{ \AA}^{-1} \times 0.1 \text{ meV}$  resolution. An additional benefit of this binning is that it allowed us not to worry about resolution effects. The lower 0.5 meV energy transfer range, that contains the elastic-incoherent and possibly phonon scattering, was excluded from the fits.

## 2. Analysis of $\text{PbNi}_2\text{V}_2\text{O}_8$ data.

For The Pb-compound the adjustable parameters were the two intrinsic gap energies  $\Delta_{\parallel}$  and  $\Delta_{\perp}$ , and the doublet 3D gap  $E_{\min,\perp}$ . The singlet 3-D gap was fixed to  $E_{\min,\parallel} = 1.2 \text{ meV}$ , as determined in high-field bulk measurements.<sup>9</sup> The only additional parameter was an overall scale factor. The least-squares refinement yields:  $\Delta_{\perp} = 4.0 \pm 0.25 \text{ meV}$ ,  $\Delta_{\parallel} = 3.1 \pm 0.3 \text{ meV}$  and  $E_{\perp}^{(\min)} = 2.4 \pm 0.2 \text{ meV}$  ( $J_1 < 0$ ), with  $\chi^2 = 2.3$ . The resulting fit is shown in Fig. 9. Substituting the obtained values into the expression for  $S(\mathbf{Q}, \omega)$ , performing a powder average and convoluting the result with the spectrometer resolution function, reproduces the measured 3-axis const- $E$  and const- $Q$  scans rather well, as shown in solid lines in Figs. 6b,7. The relatively large  $\chi^2$  of the global fit to the ASD data is to be attributed to systematic error, primarily due to “spurious” scattering. In particular, the data are partially contaminated by spurions of type “ $k_i \rightarrow k_i$ ” and “ $k_f \rightarrow k_f$ ” originating from the stronger Bragg powder lines from the sample. Areas that are affected by these spurious processes are shown as shaded “streaks” in Fig. 5. Another prominent streak in the data is to the left from, and parallel to, the two shaded areas. The origin of this feature is not known. It is however resolution-limited and temperature-independent, and is thus almost certainly spurious and of non-magnetic origin. Considering that this type of systematic error is unavoidable in powder experiments, the obtained model fit to the data is quite acceptable.

The refined value for  $E_{\min,\perp}$  is in very good agreement with the result of high-field measurements.<sup>9</sup> The interchain coupling constants are obtained from Eqs. 18,19:  $J_{1,\perp} = -0.18 \text{ meV}$  and  $J_{1,\parallel} = -0.14 \text{ meV}$ . Note that  $|J_1|$  is larger by a factor of 1.5–2, compared to our previous estimate ( $J_{\perp} = 0.096 \pm 0.003 \text{ meV}$ ) in Ref. 9. This discrepancy should be partly attributed to a difference in the definition of  $J_1$ . In our previous model each spin was coupled to 4 spins in adjacent chains (coordination number 4). In the present model the inter-chain coordination number is 2. This automatically translates into a factor of 2 for  $|J_1|$ . The negative sign of  $J_1$  indicates that this coupling is actually ferromagnetic. Note, however, that in our model  $J_1$  couples spins offset by  $c/4$  along the chain axis, so that the effective mean field coupling between interacting chains is still antiferromagnetic, as in our previous model. The 3-D magnetic zone-center, where transverse dispersion is a minimum, is at  $(1, 1, 2)$ . From the refined  $\Delta_{\perp}$  and  $\Delta_{\parallel}$  we can also get the in-chain coupling constant:  $J \approx 9.0 \text{ meV}$ . This value is in a better agreement with the high-temperature susceptibility estimate  $J \approx 8.2 \text{ meV}$  in Ref. 9, than our preliminary neutron result  $J = 9.5 \text{ meV}$ , from the same reference. The anisotropy constant  $D$  can be estimated from  $\Delta_{\perp}$  and  $\Delta_{\parallel}$  using Eqs. 16,17. For  $\text{PbNi}_2\text{V}_2\text{O}_8$  we get  $D = -0.45 \text{ meV}$ .

To convince the reader that the  $J_1$  is in fact a relevant parameter, we have performed simulations of the dynamic structure factors using the same values  $\Delta_{\perp} = 4.0 \pm 0.25 \text{ meV}$ ,  $\Delta_{\parallel} = 3.1 \pm 0.3 \text{ meV}$ , as determined in the analysis of the ASD data, but with the sign of  $J_1$  reversed:  $J_{1,\perp} = 0.18 \text{ meV}$  and  $J_{1,\parallel} = 0.14 \text{ meV}$ . The resulting simulated powder cross section is visualized in Fig. 10a, and is clearly very different from the inelastic intensity measured experimentally.

Similarly, Fig. 10b shows a simulation with  $J_{1,\perp} = J_{1,\parallel} = 0$  meV.  $J_1$  has a particular impact on the shape of the constant-energy powder scans. The dashed lines in Fig. 6 are simulations for uncoupled chains. The well-defined intensity maximum seen in the data at  $|Q| \approx 1.2 \text{ \AA}^{-1}$ , is replaced with a broad monotonous feature for uncoupled chains. In contrast, the interacting chain model reproduces the peak rather well.

### 3. Analysis of $\text{SrNi}_2\text{V}_2\text{O}_8$ data

Similar data analysis was performed for  $\text{SrNi}_2\text{V}_2\text{O}_8$ .  $E_{\parallel}^{(\min)}$  in this case was fixed at zero value (see discussion in the theory section below). The best fit to the ASD data is obtained with  $\Delta_{\perp} = 3.9 \pm 0.3$  meV,  $\Delta_{\parallel} = 2.8 \pm 0.4$  meV and  $E_{\perp}^{(\min)} = 2.35 \pm 0.3$  meV with  $\chi^2 = 2.0$ , and is shown in Fig. 9b. These values correspond to interchain coupling constants  $J_{1,\perp} = -0.18$  meV and  $J_{1,\parallel} = -0.15$  meV, respectively, almost identical to the corresponding  $\text{PbNi}_2\text{V}_2\text{O}_8$  values. An important consistency check is that using the gap values to estimate  $J$  gives almost the same value as for  $\text{PbNi}_2\text{V}_2\text{O}_8$ , as expected:  $J = 8.6$  meV. The easy-axis anisotropy constant in  $\text{SrNi}_2\text{V}_2\text{O}_8$  is larger than in  $\text{PbNi}_2\text{V}_2\text{O}_8$ :  $D = -0.56$  meV. Simulations for constant- $E$  and constant- $Q$  scans measured for  $\text{SrNi}_2\text{V}_2\text{O}_8$  in the standard 3-axis mode are shown in solid lines in Figs. 6a,8.

### 4. Observation of actual spin gaps at the 3D magnetic zone-center

From the point of view of spin dynamics, the main distinction between the singlet-ground-state  $\text{PbNi}_2\text{V}_2\text{O}_8$  and the magnetically ordered  $\text{SrNi}_2\text{V}_2\text{O}_8$  is the presence of a spin gap in the former system, and a gapless excitation spectrum in the latter. The gap is directly accessible experimentally at the 3-D AF zone-center, where the dispersion of magnetic excitations is a global minimum. As mentioned above, for both vanadates the 3D zone-center is at  $\mathbf{Q}^{(0)} = (1, 1, 2)$ , which corresponds to a momentum transfer  $|\mathbf{Q}^{(0)}| \approx 1.67 \text{ \AA}^{-1}$ . Constant- $Q$  scans extracted from our ASD data for this momentum transfer, as well as a standard  $E_f = 5$  meV constant- $Q$  scan at this wave vector, are shown in Fig. 11. To better understand these data, we note that near the 3D zone-center the single-mode contribution to the dynamic structure factor, independently of the details of the spin Hamiltonian, should be of the following form:

$$S(\mathbf{Q}, \omega) \propto \frac{1}{\omega_{\mathbf{Q}}} \delta(\omega - \omega_{\mathbf{Q}}), \quad (20)$$

$$(\hbar\omega_{\mathbf{Q}})^2 = \Delta^2 + v_{\parallel}^2(Q_{\parallel} - Q_{\parallel}^{(0)})^2 + v_{\perp}^2(Q_{\perp} - Q_{\perp}^{(0)})^2.$$

In this formula  $\Delta$  is the gap energy, and  $v_{\parallel}$  and  $v_{\perp}$  are spin wave velocities along and perpendicular to the chain axis  $c$ , respectively. The data shown in Fig. 11c were collected with a horizontally-focusing analyzer. At energy transfers below 1 meV in this mode we are picking up a great deal of diffuse and phonon scattering (  $(1, 1, 2)$  is an allowed nuclear Bragg peak !). Above this contaminated region though, in a powder sample we effectively observe a  $\mathbf{Q}$ -integral of the cross-section around the 3D zone-center. The same applies to the scans in Figs. 11a and b, where integration was performed in the range  $1.6\text{--}1.7 \text{ \AA}^{-1}$ . For the  $Q$ -integrated intensity Eq. 20 gives:

$$S(\omega) \propto \sqrt{\omega^2 - \Delta^2}. \quad (21)$$

The linear increase of intensity seen for  $\text{SrNi}_2\text{V}_2\text{O}_8$  in Fig. 11 should thus indeed be interpreted as due to a gapless spin wave ( $\Delta = 0$ ). In contrast, for  $\text{PbNi}_2\text{V}_2\text{O}_8$ , the threshold behavior is a clear sign of an energy gap. These effects are also seen in constant- $Q$  scans extracted from the ASD data by binning the pixels in a  $0.1 \text{ \AA}^{-1}$   $Q$ -range.

### C. $\text{SrNi}_2\text{V}_2\text{O}_8$ : Temperature dependence

To better understand the mechanism of long-range ordering of  $\text{SrNi}_2\text{V}_2\text{O}_8$  we studied the temperature dependence of inelastic scattering at the momentum transfer  $|\mathbf{Q}^{(0)}| = 1.67 \text{ \AA}^{-1}$  in this compound. Typical data are shown in Fig. 12. The solid lines were obtained by fitting our model cross section to the data at each temperature. The lower 0.75 meV energy transfer range was excluded from this analysis, as the difficult-to-estimate phonon contribution in this range is expected to increase dramatically with increasing  $T$ . The set of independent parameters was slightly modified. The anisotropy splitting of the triplet  $D$ , as well as both inter-chain coupling constants  $J_{1,\perp}$  and  $J_{1,\parallel}$  were fixed at the values determined at  $T = 1.5$  K. The mean gap  $\langle\Delta\rangle$  and an intensity prefactor were refined to best-fit

the scans at each temperature. The obtained temperature dependences are shown in Fig. 13. As previously observed in other Haldane-gap systems,  $\langle \Delta \rangle$  increases with increasing  $T$ . Even though this change is rather small, according to Eqs. 18,19, it corresponds to an appreciable variation of the gap in the longitudinal mode (Fig. 14). Upon cooling, the longitudinal gap approaches zero at  $T = T_N$ , which results in a soft-mode transition to a magnetically ordered state. This type of behavior is very similar to that found in  $\text{CsNiCl}_3$ .<sup>3-5</sup>

## V. THEORY AND DISCUSSION

### A. Derivation of the model cross section

To calculate the effect of weak inter-chain interactions on dynamic spin correlations in  $\text{PbNi}_2\text{V}_2\text{O}_8$  and  $\text{SrNi}_2\text{V}_2\text{O}_8$  we shall use the Random Phase Approximation (RPA).<sup>17</sup> This approach for directly coupled Haldane spin chains has been successfully applied, for example, to  $\text{CsNiCl}_3$  (Ref. 4). More recently it was shown to also work well for Haldane chains coupled via classical spins.<sup>18</sup> The only additional difficulties in the present case arise from the complicated 3-D arrangement of magnetic ions in the  $\text{PbNi}_2\text{V}_2\text{O}_8$  structure, and from the rather non-trivial geometry of interchain coupling. To somewhat simplify the task we shall break it up into two distinct problems. First, we shall worry only about the *topology* of magnetic interactions and consider an equivalent Bravais lattice of spins, assuming straight spin chains and a system of inter-chain bonds shown in Fig. 4b. Making use of the general RPA equations for coupled spin chains, summarized in Appendix I, we shall write down the RPA susceptibility and dynamic structure factor  $S'(\mathbf{Q}, \omega)$  for this model. In a separate step we shall adapt the result to the more complex structure of  $\text{PbNi}_2\text{V}_2\text{O}_8$ , using the formulas of Appendix II.

#### 1. Structure factor for an equivalent Bravais lattice

The first step in the RPA calculation is to write down the bare (non-interacting) susceptibility for an isolated Haldane spin chain, for which the single-mode approximation (SMA) is known to work rather well:<sup>12-14</sup>

$$\chi_0(\mathbf{Q}, \omega) = \frac{1 - \cos(Q_z c/4)}{2} \frac{Zv}{\Delta^2 + v^2 \sin^2(Q_z c/4) - (\hbar\omega + i\epsilon)^2} \quad (22)$$

This expression should be used separately for each channel of spin polarization, with appropriate values of gap energy  $\Delta$  for each particular mode.

Expression 22 is to be substituted in the general RPA equations 33. Even for the “straightened out” spin chains in Fig. 4b there are still 16 spins per unit cell, so we end up with 16 couple equations and 16 modes for each polarization! For the low-energy part of the excitation spectrum it is however quite appropriate to use the approximation of Eqs. 34. This reduces the problem to only 4 self-consistent RPA equations (there are 4 spin chains in each crystallographic unit cell). Moreover, at this level of approximation the set of 4 RPA equations is degenerate, and we end up with a single RPA equation for each polarization:

$$\chi_{\text{RPA}}^{-1}(\mathbf{Q}) = \chi_0^{-1}(\mathbf{Q}) [\chi_0(\mathbf{Q}) \mathcal{J}(\mathbf{Q}) + 1], \quad (23)$$

where

$$\mathcal{J}(\mathbf{Q}) = J_1 \cos(Q_z c/4) [\cos(Q_x a/2) + \cos(Q_y a/2)]. \quad (24)$$

This equation is easily solved analytically. By taking the imaginary part of the thus obtained  $\chi_{\text{RPA}}(\mathbf{Q})$  we arrive at Eqs. 12–15.

#### 2. Actual structure

The transformation from the Bravais spin lattice (straight chains) to the spiral-chain structure of  $\text{PbNi}_2\text{V}_2\text{O}_8$  and  $\text{SrNi}_2\text{V}_2\text{O}_8$  is schematized in Fig. 15. This figure also serves as an illustration of the notation used in Appendix I. Applying Eq. 44 is straightforward, and we will spare the reader the tedious calculations. The final relation between  $S(\mathbf{q}, \omega)$  and  $S'(\mathbf{q}, \omega)$  is as in Eqs. 6,9.

## B. Temperature effects

### 1. Disordered phase

The derivation above can be repeated almost verbatim for the case  $T > 0$ . Temperature enters RPA calculation indirectly, through an intrinsic temperature dependence of bare susceptibilities of individual chains (Eq. 22). Two effects at  $T > 0$  need be considered: i) the increase of the Haldane gap, compared to its  $T = 0$  value, and ii) damping of Haldane excitations. Both phenomena have been observed in a number of model quasi-1-D systems (see, for example, Refs. 19–21). Unfortunately, it is almost impossible to extract meaningful information regarding excitation lifetimes from powder inelastic data. As most of the observed inelastic signal originates from excitations with energies greater than 2 meV, the temperature dependence of the intrinsic Haldane gap is much easier to observe. For this reason we analyzed the temperature dependence of the inelastic signal measured in  $\text{SrNi}_2\text{V}_2\text{O}_8$  using the same single-mode approximation (Eq. 22), as at base temperature (see fits in Fig. 12), to obtain the  $T$ -dependences of intrinsic Haldane gap energies (Fig. 13). From the mapping of the Heisenberg Hamiltonian on the quantum non-linear  $\sigma$ -model (NLSM) one expects a rather steep increase of the gap energy with increasing temperature:<sup>22</sup>

$$\Delta(T) \approx \Delta(0) + \sqrt{2\pi} \sqrt{T\Delta(0)} \exp\left(-\frac{\Delta(0)}{k_B T}\right). \quad (25)$$

The actual increase of the gap energy observed experimentally NENP,<sup>19</sup> NINAZ,<sup>20</sup> and  $\text{Y}_2\text{BaNiO}_5$ ,<sup>21</sup> was found to be consistently smaller than this NLSM prediction. The same discrepancy, namely a rather slow increase of the gap energy with temperature, is seen in  $\text{SrNi}_2\text{V}_2\text{O}_8$  as well. Equation 25 is plotted in a dashed line in Fig. 13a. The solid line is an empirical fit in which the prefactor  $\sqrt{2\pi}$  in Eq. 25 was replaced by an adjustable parameter  $A$ . For  $\text{SrNi}_2\text{V}_2\text{O}_8$  we get  $A = 0.67(1) \ll \sqrt{2\pi}$ . A self-consistency check for our SMA model is that the refined intensity prefactor is almost  $T$ -independent, as shown in Fig. 13b. In other words, the decrease of actual excitation intensity is entirely due to the increase of gap energy, and the intensity scales as  $1/\omega$ .

In  $\text{SrNi}_2\text{V}_2\text{O}_8$  the ordering temperature  $T_N = 7$  K is significantly smaller than the intrinsic Haldane gap energy  $\Delta \approx 4$  meV. As both the gap energy and excitation width are expected to increase exponentially with  $T$ , such a small  $T_N$  suggests that inter-chain interactions in  $\text{SrNi}_2\text{V}_2\text{O}_8$  are barely strong enough to produce a LRO-ground state. Long-range ordering in  $\text{SrNi}_2\text{V}_2\text{O}_8$ , and the absence of such in  $\text{PbNi}_2\text{V}_2\text{O}_8$ , are a very “lucky” coincidence that results from a fine interplay between in-chain interaction strength, magnetic anisotropy and inter-chain coupling.

### 2. Magnetically ordered state

Our model cross section was derived under the implicit assumption that the system is in a non-magnetic state, which is *not* applicable to  $\text{SrNi}_2\text{V}_2\text{O}_8$  at  $T < T_N$ . In this regime one expects an *increase* of the gap energies, at least for the longitudinal mode, due to the presence of a mean static staggered field generated by the ordered staggered moment in the system.<sup>23,24</sup> To adapt the MF-RPA calculation to this temperature regime one has to know the ordered moment in the system. To date, powder diffraction experiments on  $\text{SrNi}_2\text{V}_2\text{O}_8$  failed to detect any magnetic Bragg reflections in this compound at low temperatures,<sup>25</sup> and the magnetic order parameter is thus expected to be very small. This is consistent with our previous observation that the system is “barely” 3-dimensional enough to become ordered at low temperatures. Provided the ordered moment is small, within the accuracy of our powder experiments it seems quite appropriate to use the same cross section for  $T < T_N$ , as for the paramagnetic phase, and postulate  $E_{\min,\parallel} = 0$ . This assumption is equivalent to assuming  $T_N = 0$ .

### 3. Placement on the phase diagram

The line of quantum phase transition separating the ordered and spin-liquid states can be derived from Eqs. 16-19. The critical value for  $J_1$  corresponds to the lower gap energy (in our case  $E_{\min,\parallel}$ ) being equal to zero. The resulting phase diagram is very similar to the direct numerical calculations by Sakai and Takashi,<sup>7</sup> and is shown in Fig. 1. Using the results for  $\text{PbNi}_2\text{V}_2\text{O}_8$  and  $\text{SrNi}_2\text{V}_2\text{O}_8$  described above, we are able to place the two new materials on the same plot. It has to be emphasized, that for  $\text{SrNi}_2\text{V}_2\text{O}_8$  the parameters  $D$  and  $J_1$  were extracted from the experimental data using a cross-section for a disordered system, and assuming  $E_{\min,\parallel} \equiv 0$ . That  $\text{SrNi}_2\text{V}_2\text{O}_8$  lands *exactly* on the phase boundary is thus an artifact of our data analysis procedure. In reality,  $\text{SrNi}_2\text{V}_2\text{O}_8$  must be positioned slightly above the phase boundary. The disordered  $\text{PbNi}_2\text{V}_2\text{O}_8$  is not influenced by such an artifact, and its positioning can be considered quite reliable.



## VI. SUMMARY

Our neutron scattering results help explain the different ground state properties of the two very similar vanadates. The ratio of inter-chain to in-chain coupling in  $\text{SrNi}_2\text{V}_2\text{O}_8$  is slightly larger than in  $\text{PbNi}_2\text{V}_2\text{O}_8$ .  $\text{SrNi}_2\text{V}_2\text{O}_8$  is also driven towards LRO by the somewhat larger magnetic anisotropy. The quantitative data analysis enables us to precisely position the two compounds on the Sakai-Takahashi phase diagram, just opposite to each other relative to the ordered-disordered phase boundary. This almost unbelievable coincidence opens many exciting possibilities for future studies. Experiments on aligned powders will enable more accurate measurements of the excitation spectrum near the 3D zone-center. High-pressure studies, as previously attempted for NENP,<sup>26</sup> may lead to the first observation of pressure-induced long-range ordering in a quantum-disordered magnet.

## ACKNOWLEDGMENTS

We would like to thank Y. Sasago, who has suggested at the early stage of this study that  $\text{SrNi}_2\text{V}_2\text{O}_8$  may be a Haldane-gap antiferromagnet. We also thank R. Wickmann for sending a copy of Ref. 11. Work at the University of Tokyo was supported in part by Grant-in-Aid for COE Research “Phase Control of Spin-Charge-Phonon Coupled Systems” from the Ministry of Education, Science, Sports and Culture of Japan. Work at Brookhaven National Laboratory was carried out under Contract No. DE-AC02-76CH00016, Division of Material Science, U.S. Department of Energy. Studies at NIST were partially supported by the NSF under contract No. DMR-9413101.

## APPENDIX I: RPA SUSCEPTIBILITY FOR WEAKLY COUPLED SPIN CHAINS

The general RPA technique of calculating the dynamic susceptibility and structure factor for weakly interacting systems is well established and documented (see, for example, Ref. 27). In particular, the approach has been on many occasions applied to weakly coupled quantum spin chains.<sup>17,4</sup> In the present section, without any claims of novelty, and for reference only, we shall derive some useful RPA results for weakly coupled spin chains assuming a rather general geometry of inter-chain bonding. Note that the notation used in this Appendix is totally independent from that in the rest of the paper.

We consider a crystal structure composed of identical parallel uniform spin chains that run along the  $\mathbf{a}$  axis. The spacing between spins in each chain is  $a/K$ , where  $K$  is integer. There are  $M$  chains in each crystallographic unit cell. The origin of the  $m$ -th chain is at  $\mathbf{R}_n + \boldsymbol{\rho}_m$ . The position of the  $i$ -th spin in chain  $(n, m)$  can be written as  $\mathbf{R}_n + \boldsymbol{\rho}_m + i\mathbf{a}/K$ . A single crystallographic unit cell thus contains  $MK$  spins. For convenience we shall break up the in-chain spin index  $i$  into two:  $i = lK + k$ ,  $0 \leq k < K$ . The spin Hamiltonian for inter-chain interactions will be written as:

$$\hat{H}_{\text{interchain}} = \sum_{n,n'} \sum_{m,m'} \sum_{l,l'} \sum_{k=0}^{K-1} \sum_{k'=0}^{K-1} s_{l,k}^{(n,m)} s_{k',l'}^{(n',m')} J(n, n', m, m', Kl + k, Kl' + k') \quad (26)$$

We assume all exchange interactions to be simultaneously diagonal in spin projection indexes. All the equations in this section thus apply to a particular channel of spin polarization. In our model the exchange constant satisfies certain translational-symmetry relations:

$$J(n, n', m, m', Kl + k, Kl' + k') = J((\mathbf{R}_{n'} - \mathbf{R}_n), m, m', (l' - l), k, k'). \quad (27)$$

In order to write down self-consistent RPA equations, we have to answer the following question. Suppose we have artificially induced a spin density  $s^{(m')}(\mathbf{r})$  (or, equivalently,  $s^{(m')}(\mathbf{q})$ ) in the chain-sublattice  $m'$ . What exchange field will this spin density project on the chains in sublattice  $m$ ? By definition, the exchange field acting on spin  $s_{l,k}^{(n,m)}$  is given by:

$$h_{l,k}^{(n,m)} = \sum_{n'} \sum_{m'=0}^{M-1} \sum_{l'} \sum_{k'=0}^{K-1} s_{l',k'}^{(n',m')} J((\mathbf{R}_{n'} - \mathbf{R}_n), m, m', (l' - l), k, k') \quad (28)$$

We, of course, will be interested in the Fourier transform of the exchange field acting on sublattice  $m$ :

$$h^{(m)}(\mathbf{q}) \equiv \sum_n \sum_l \sum_{k=0}^{K-1} h_{l,k}^{(n,m)} \exp[-i\mathbf{q}(\mathbf{R}_n + \boldsymbol{\rho}_m + \mathbf{a}(k/K + l))]. \quad (29)$$

Having introduced the definition

$$J_{k,m,m'}(\mathbf{q}) \equiv \sum_{n,k',l} \exp[-i\mathbf{q}(\mathbf{R}_n + \boldsymbol{\rho}_{m'} - \boldsymbol{\rho}_m + \mathbf{a}l + \mathbf{a}(k' - k)/K)] J(\mathbf{R}_n, m', m, l, k', k), \quad (30)$$

it is straightforward to verify that:

$$h^{(m)}(\mathbf{q}) = \sum_{m'=0}^{M-1} \sum_{\kappa=0}^{K-1} \mathcal{J}_{\kappa,m,m'}(\mathbf{q}) s^{(m')}(\mathbf{q} + \kappa \mathbf{a}^*), \quad (31)$$

where

$$\mathcal{J}_{\kappa,m,m'}(\mathbf{q}) \equiv \frac{1}{K} \sum_k J_{k,m,m'}(\mathbf{q}) \exp[2\pi i \kappa k / K]. \quad (32)$$

Equation 31 enables us to immediately write down the self-consistent RPA equations:

$$\chi^{(m)}(\mathbf{q}, \omega) = \left[ \sum_{m'=0}^{M-1} \sum_{\kappa=0}^{K-1} \chi_0^{(m')}(\mathbf{q} + \kappa \mathbf{a}^*, \omega) \mathcal{J}_{\kappa,m,m'}(\mathbf{q}) + 1 \right]^{-1} \chi_0^{(m)}(\mathbf{q}, \omega). \quad (33)$$

Here  $\chi_0^{(m)}(\mathbf{q}, \omega)$  and  $\chi^{(m)}(\mathbf{q}, \omega)$  are the bare (non-interacting) and RPA-corrected wave vector dependent dynamic susceptibilities of spin chains in the  $m$ -th sublattice, respectively. For any wave vector  $\mathbf{q}$  one obtains  $KM$  equations: susceptibilities at  $K$  wave vectors become coupled to each other and there are  $M$  independent chain-sublattices.

For a Heisenberg AF chain, at energy transfers much smaller than the in-chain exchange constant,  $\chi_0^{(m)}(\mathbf{q})$  is typically very small except when momentum transfer along the chain axis is close to  $q_0$ , defined by  $q_0 a = \pi$ . To a good approximation we can thus replace Eq. 33 with:

$$\begin{aligned} \chi^{(m)}(\mathbf{q} \mathbf{a} \sim \pi, \omega) &\approx \left[ \sum_{m'=1}^M \chi_0^{(m')}(\mathbf{q}, \omega) J_{m,m'}(\mathbf{q}) + 1 \right]^{-1} \chi_0^{(m)}(\mathbf{q}, \omega), \\ \chi^{(m)}(\mathbf{q} \mathbf{a} \neq \pi, \omega) &\approx 0, \end{aligned} \quad (34)$$

where

$$J_{m,m'}(\mathbf{q}) \equiv \frac{1}{K} \sum_n \sum_l \sum_{k=1}^K \sum_{k'=1}^K J(\mathbf{R}_n, m, m', l, k, k') \exp[-i\mathbf{q}(\mathbf{R}_n + \mathbf{a}l + \mathbf{a}(k' - k)/K + (\boldsymbol{\rho}_{m'} - \boldsymbol{\rho}_m))] \quad (35)$$

is simply the Fourier transform of exchange interactions between sublattices  $m$  and  $m'$ . Note that there are only  $M$  equations in the system 34.

## APPENDIX II: EQUIVALENT BRAVAIS LATTICE

In this section we shall derive a useful relation between magnetic dynamic structure factors of two spin lattices described by the same Hamiltonian, but featuring different 3D arrangements of magnetic sites. Lattice I is assumed to be a simple Bravais lattice of magnetic sites and consists of  $N$  unit cells of volume  $v$ . The origin of the  $n$ -th unit cell  $\mathbf{R}_n^{(I)}$  coincides with the position of the  $n$ -th spin:  $\mathbf{r}_n^{(I)} \equiv \mathbf{R}_n^{(I)}$ . Unlike lattice I, lattice II is non-Bravais, having  $M$  spins per unit cell, and a unit cell volume  $V = Mv$ . There are  $K = N/M$  unit cells with origins at  $\mathbf{R}_k^{(II)}$ , respectively. Lattice II is obtained from lattice I by shifting each spin  $n$  by  $\boldsymbol{\rho}_n$ . In lattice II the spins are thus positioned at  $\mathbf{r}_n^{(II)} \equiv \mathbf{r}_n^{(I)} + \boldsymbol{\rho}_n$ . The relation between the two lattices allows us to write  $\mathbf{r}_n^{(II)} = \mathbf{R}_k^{(II)} + \mathbf{r}_m^{(II)} = \mathbf{R}_k^{(II)} + \mathbf{r}_m^{(I)} + \boldsymbol{\rho}_m$  ( $n = kM + m$ ,  $0 \leq m < M$ ). We assume the spin systems to be equivalent in the sense that the spin Hamiltonian of system II written in terms of site-spin operators  $\hat{\mathbf{s}}_n$  is identical to that of system I. The notation introduced above

is independent of that used in the rest of the paper or in Appendix I, and is illustrated, for the particular case of  $\text{PbNi}_2\text{V}_2\text{O}_8$ , in Fig. 15.

The Fourier transform of the total spin operator for lattice I is defined as:

$$s^{(I)}(\mathbf{q}) = \sum_{n=0}^{N-1} s_n \exp[-i\mathbf{q}\mathbf{R}_n^{(I)}] = \sum_{k=0}^{K-1} \sum_{m=0}^{M-1} s_{kM+m} \exp[-i\mathbf{q}(\mathbf{R}_{kM}^{(I)} + \mathbf{r}_m^{(I)})]. \quad (36)$$

Again, for simplicity, we have omitted the spin projection indexes. The reverse relation is given by:

$$s_{kM+m} = \frac{v}{(2\pi)^3} \int d\mathbf{q} s^{(I)}(\mathbf{q}) \exp[i\mathbf{q}(\mathbf{R}_{kM}^{(I)} + \mathbf{r}_m^{(I)})], \quad (37)$$

where the integral is taken over the Brillouin zone of the Bravais lattice ( a reciprocal-space volume  $K$  times as large as the Brillouin zone of the lattice II). Similarly, for lattice II, by definition:

$$s^{(II)}(\mathbf{q}) = \sum_{k=0}^{K-1} \sum_{m=0}^{M-1} s_{kM+m} \exp[-i\mathbf{q}(\mathbf{R}_k^{(II)} + \mathbf{r}_m^{(II)})]. \quad (38)$$

The equivalence of the two systems allows us to directly combine the last two equations:

$$s^{(II)}(\mathbf{q}) = \frac{v}{(2\pi)^3} \sum_{k=0}^{K-1} \sum_{m=0}^{M-1} \exp[-i\mathbf{q}(\mathbf{R}_k^{(II)} + \mathbf{r}_m^{(II)})] \int d\mathbf{p} \exp[i\mathbf{p}(\mathbf{R}_{kM}^{(I)} + \mathbf{r}_m^{(I)})] s^{(I)}(\mathbf{p}). \quad (39)$$

The expression can be simplified by noting that

$$\sum_{k=0}^{K-1} \exp[-i(\mathbf{q} - \mathbf{p})\mathbf{R}_k^{(II)}] = \frac{(2\pi)^3}{V} \sum_{\mathbf{T}} \delta(\mathbf{p} - \mathbf{q} - \mathbf{T}). \quad (40)$$

Here the inner sum is taken over reciprocal-lattice points  $\mathbf{T}_k$ ,  $k = 0 \dots K$ , for lattice II. Plugging this result into the expression into Eq. 39 gives:

$$\begin{aligned} s^{(II)}(\mathbf{q}) &= \frac{v}{V} \int d\mathbf{p} s^{(I)}(\mathbf{p}) \sum_{\mathbf{T}} \delta(\mathbf{p} - \mathbf{q} - \mathbf{T}) \sum_{m=1}^{M-1} \exp[-i(\mathbf{q}\mathbf{r}_m^{(II)} - \mathbf{p}\mathbf{r}_m^{(I)})] \\ &= \frac{1}{M} \sum_{m=0}^{M-1} \exp(-i\mathbf{q}\mathbf{r}_m) \sum_{\mu=1}^{M-1} s^{(I)}(\mathbf{q} + \mathbf{T}_\mu) \exp(i\mathbf{T}_\mu\mathbf{r}_m^{(I)}) \end{aligned} \quad (41)$$

In this the last expression the first sum is taken over all reciprocal-lattice vectors  $\mathbf{T}_\mu$  of lattice II within the first Brillouin zone of lattice I.

Equation 41 for the Fourier transform of spin operators can now be directly plugged into the definition of dynamic structure factors for the two lattices:

$$S^{(I)}(\mathbf{q}, \omega) \equiv \frac{1}{2\pi\hbar} \int dt \exp(-i\omega t) \langle s^{(I)}(-\mathbf{q}, 0) s^{(I)}(\mathbf{q}, t) \rangle \quad (42)$$

$$S^{(II)}(\mathbf{q}, \omega) \equiv \frac{1}{2\pi\hbar} \int dt \exp(-i\omega t) \langle s^{(II)}(-\mathbf{q}, 0) s^{(II)}(\mathbf{q}, t) \rangle. \quad (43)$$

A straightforward, though somewhat tedious calculation gives the result that we were after:

$$S^{(II)}(\mathbf{q}, \omega) = \sum_{\mu=0}^{M-1} \left| \sum_{m=0}^{M-1} \exp(-i\mathbf{q}\mathbf{r}_m) \exp(i\mathbf{T}_\mu\mathbf{r}_m^{(I)}) \right|^2 S^{(I)}(\mathbf{q} + \mathbf{T}_\mu, \omega) \quad (44)$$

- <sup>1</sup> F. D. M. Haldane, Phys. Rev. Lett. **50**, 1153 (1983).
- <sup>2</sup> F. D. M. Haldane, Phys. Lett. **93A**, 464 (1983).
- <sup>3</sup> W. J. L. Buyers, *et al.*, Phys. Rev. Lett. **56** 371 (1986); M. Enderle, Z. Tun, W. J. L. Buyers, and M. Steiner, Phys. Rev. B **59**, 4235 (1999), and references therein. and references therein.
- <sup>4</sup> R. M. Morra, W. J. L. Buyers, R. L. Armstrong, and K. Hirakawa, Phys. Rev. B **38**, 543 (1988).
- <sup>5</sup> T. Inami, K. Kakurai, H. Tanaka, M. Enderle, and M. Steiner, J. Phys. Soc. Japan **63**, 1530 (1994); M. Enderle, K. Kakurai, M. Steiner, and H. Weinfurter, J. Magn. Magn. Mat. **104–107**, 809 (1992); M. Enderle *et al.*, Europhys. Lett. **25**, 717 (1994).
- <sup>6</sup> I. Zaliznyak, L.-P. Regnault, and D. Petitgrand, Phys. Rev. B **50**, 15824 (1994).
- <sup>7</sup> T. Sakai and M. Takahashi, Phys. Rev. B **42**, 4537 (1990).
- <sup>8</sup> Z. Tun, W. J. L. Buyers, A. Harrison, and J. A. Rayne, Phys. Rev. B **43**, 13331 (1991).
- <sup>9</sup> Y. Uchiyama *et al.*, Phys. Rev. Lett. **83**, 632 (1999).
- <sup>10</sup> Y. Uchiyama, unpublished X-ray diffraction data.
- <sup>11</sup> R. Wickman and H. Müller-Buschbaum, Revue de Chimie minérale **23**, 1 (1986).
- <sup>12</sup> D. P. Arovas, A. Auerbach, and F. D. M. Haldane, Phys. Rev. Lett. **60**, 531 (1988).
- <sup>13</sup> G. Muller, H. Thomas, M. W. Puga, and H. Beck, J. Phys. C **14**, 3399 (1981).
- <sup>14</sup> S. Ma *et al.*, Phys. Rev. Lett. **69**, 3571 (1992).
- <sup>15</sup> E. S. Sorensen and I. Affleck, Phys. Rev. B **49**, 15771 (1994).
- <sup>16</sup> O. Golinelli, T. Jolicoeur, and R. Lacaze, Phys. Rev. B **45**, 9798 (1992).
- <sup>17</sup> Scalapino, D. J. , Imry, Y., and Pincus, P., Phys. Rev. B **11**, 2042- (1975).
- <sup>18</sup> A. Zheludev, S. Maslov, S. Raymond, T. Yokoo, K. Hirota, S. E. Nagler, and J. Akimitsu, Phys. Rev. B (submitted) BK7332 (1999); cond-mat/9910335.
- <sup>19</sup> S. Ma *et al.*, Phys. Rev. B **51**, 3289 (1995).
- <sup>20</sup> A. Zheludev *et al.*, Phys. Rev. B **53**, 15004 (1996).
- <sup>21</sup> T. Sakaguchi, K. Kakurai, T. Yokoo, and J. Akimitsu, J. Phys. Soc. Jpn. **65**, 3025 (1996).
- <sup>22</sup> T. Jolicoeur and O. Golinelli, Phys. Rev. B **50**, 9265 (1994).
- <sup>23</sup> I. Affleck, Phys. Rev. Lett. **62**, 474 (1989).
- <sup>24</sup> S. Maslov and A. Zheludev, Phys. Rev. Lett. **80**, 5786 (1998).
- <sup>25</sup> P. Boni *et al.*, unpublished neutron powder diffraction data.
- <sup>26</sup> I. Zaliznyak, D. C. Dender, C. Broholm, and D. H. Reich, Phys. Rev. B **57**, 5200 (1998).
- <sup>27</sup> J. Jensen and A. R. Mackintosh, in *Rare earth magnetism* (Clarendon Press, Oxford, 1991), Chap. 3.
- <sup>28</sup> G. Xu *et al.*, Phys. Rev. B **54**, R6827 (1996).
- <sup>29</sup> L. P. Regnault, I. Zaliznyak, J. P. Renard, and C. Vettier, Phys. Rev. B **50**, 9174 (1994).
- <sup>30</sup> H. Mutka *et al.*, Phys. Rev. Lett. **67**, 497 (1991).

FIG. 1.  $D - J_1$  Phase diagram for weakly coupled Haldane spin chains,<sup>7</sup> showing the location of some well-characterized quasi-1D  $S = 1$  systems. For each material  $J_1$  is scaled by the coordination number. CsNiCl<sub>3</sub> data from Ref. 4; Y<sub>2</sub>BaNiO<sub>5</sub> data from Ref. 28; NENP data from Ref. 29; AgVP<sub>2</sub>S<sub>6</sub> data from Ref. 30. PbNi<sub>2</sub>V<sub>2</sub>O<sub>8</sub> and SrNi<sub>2</sub>V<sub>2</sub>O<sub>8</sub> are placed based on the results of this work.

FIG. 2. (a) Crystal structure on PbNi<sub>2</sub>V<sub>2</sub>O<sub>8</sub> and SrNi<sub>2</sub>V<sub>2</sub>O<sub>8</sub>. The magnetic chains are formed by edge-sharing NiO<sub>6</sub> octahedra (dark gray) and are bridged by VO<sub>4</sub> tetrahedra (light gray). (b) A perspective view of the spiral-shaped Ni<sup>2+</sup>-chains in PbNi<sub>2</sub>V<sub>2</sub>O<sub>8</sub> and SrNi<sub>2</sub>V<sub>2</sub>O<sub>8</sub>.

FIG. 3. Geometry of inter-chain interactions in PbNi<sub>2</sub>V<sub>2</sub>O<sub>8</sub> and SrNi<sub>2</sub>V<sub>2</sub>O<sub>8</sub> (dark bonds). The strongest inter-chain coupling is assumed to be between nearest-neighbor Ni<sup>2+</sup> ions from adjacent chains. These sites are offset relative to each other by  $c/4$  along the chain axis.

FIG. 4. Topology of magnetic interactions PbNi<sub>2</sub>V<sub>2</sub>O<sub>8</sub> and SrNi<sub>2</sub>V<sub>2</sub>O<sub>8</sub>. Inter-chain bonds are shown as dashed lines. Solid lines are in-chain Ni-Ni bonds. (a): Model used in Ref. 9. (b): Model used in the present paper.

FIG. 5. False-color plot of inelastic neutron scattering intensities measured in PbNi<sub>2</sub>V<sub>2</sub>O<sub>8</sub> (a) and SrNi<sub>2</sub>V<sub>2</sub>O<sub>8</sub> (b) at  $T = 1.5$  K using an area-sensitive detector setup. The background has been subtracted, as described in the text. Shaded areas indicate the location of possible spurions.

FIG. 6. Constant-energy scans measured in  $\text{PbNi}_2\text{V}_2\text{O}_8$  (a) and  $\text{SrNi}_2\text{V}_2\text{O}_8$  (b) powder samples at  $T = 2$  K in the standard 3-axis mode. The solid lines are simulations based on parameters obtained in a global fit to the ASD data, as described in the text. Dashed lines are similar simulations for non-interacting spiral-shaped spin chains.

FIG. 7. Typical constant- $Q$  scans measured in  $\text{PbNi}_2\text{V}_2\text{O}_8$  powder sample at  $T = 2$  K in the standard 3-axis mode. The solid lines are as in Fig. 6.

FIG. 8. Typical constant- $Q$  scans measured in  $\text{SrNi}_2\text{V}_2\text{O}_8$  powder sample at  $T = 2$  K in the standard 3-axis mode. The solid lines are as in Fig. 6.

FIG. 9. Simulated inelastic scattering cross section based on parameters obtained in a global fit to the ASD data for  $\text{PbNi}_2\text{V}_2\text{O}_8$  (a) and  $\text{SrNi}_2\text{V}_2\text{O}_8$  (b).

FIG. 10. Simulated inelastic scattering cross section based on parameters obtained in a global fit to the ASD data for  $\text{PbNi}_2\text{V}_2\text{O}_8$ , assuming a reversed sign of  $J_1$  (a) and no inter-chain interactions (b).

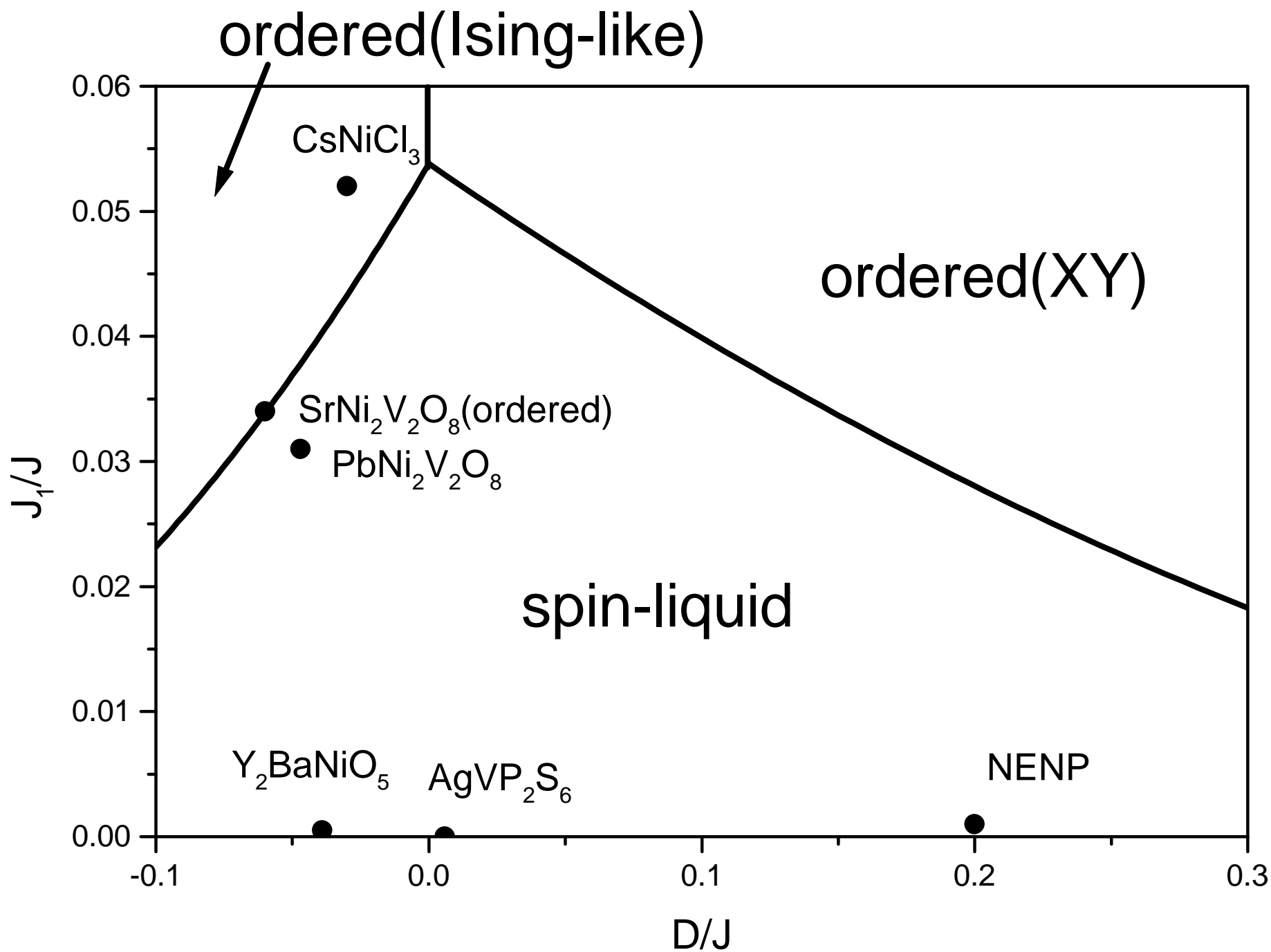
FIG. 11. Constant- $Q$  scans extracted from the ASD data sets for  $\text{PbNi}_2\text{V}_2\text{O}_8$  (a) and  $\text{SrNi}_2\text{V}_2\text{O}_8$  (b) at a momentum transfer that corresponds to the 3D antiferromagnetic zone-center (symbols). Unlike in  $\text{SrNi}_2\text{V}_2\text{O}_8$ , the measured inelastic intensity in  $\text{PbNi}_2\text{V}_2\text{O}_8$  extrapolates to zero at a non-zero energy transfer (arrows). This is even better seen in constant- $Q$  scans measured in the standard 3-axis mode (c). Open and solid symbols correspond to  $\text{SrNi}_2\text{V}_2\text{O}_8$  and  $\text{PbNi}_2\text{V}_2\text{O}_8$ , respectively. In the latter plot the data for the two compounds were brought to a single scale using the elastic incoherent signal. In all cases the solid lines are as in Fig. 6.

FIG. 12. Typical constant- $Q$  scans measured in  $\text{SrNi}_2\text{V}_2\text{O}_8$  powder at different temperatures, at a momentum transfer that corresponds to the 3D antiferromagnetic zone-center. The solid lines are fits to the model cross section, as described in the text.

FIG. 13. Measured temperature dependence of the mean intrinsic Haldane gap  $\langle\Delta\rangle$  (a) and intensity prefactor in the model cross section described in the text (b) for  $\text{SrNi}_2\text{V}_2\text{O}_8$ .

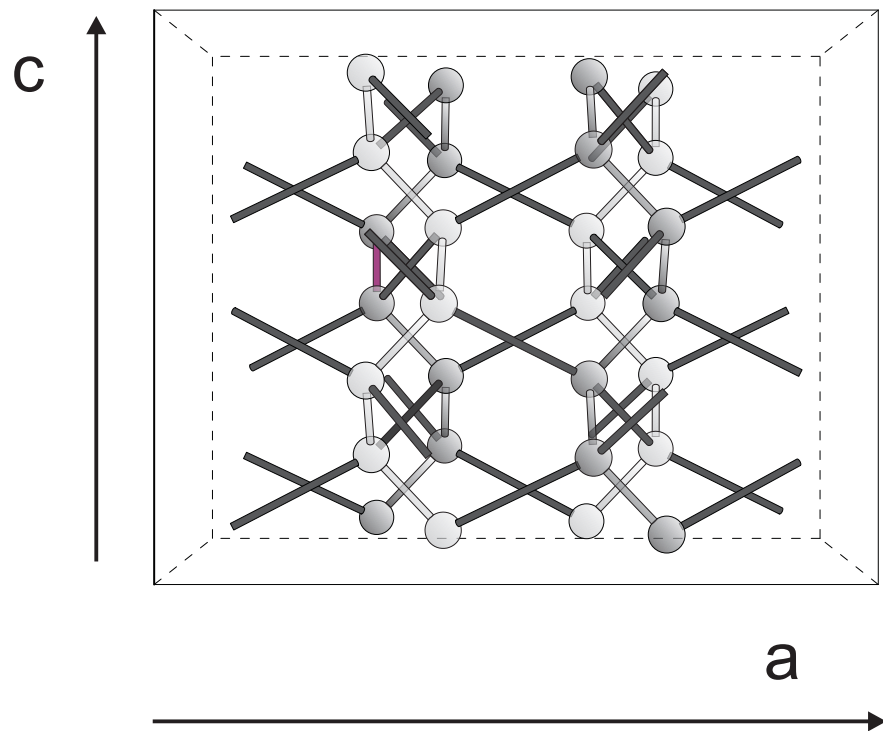
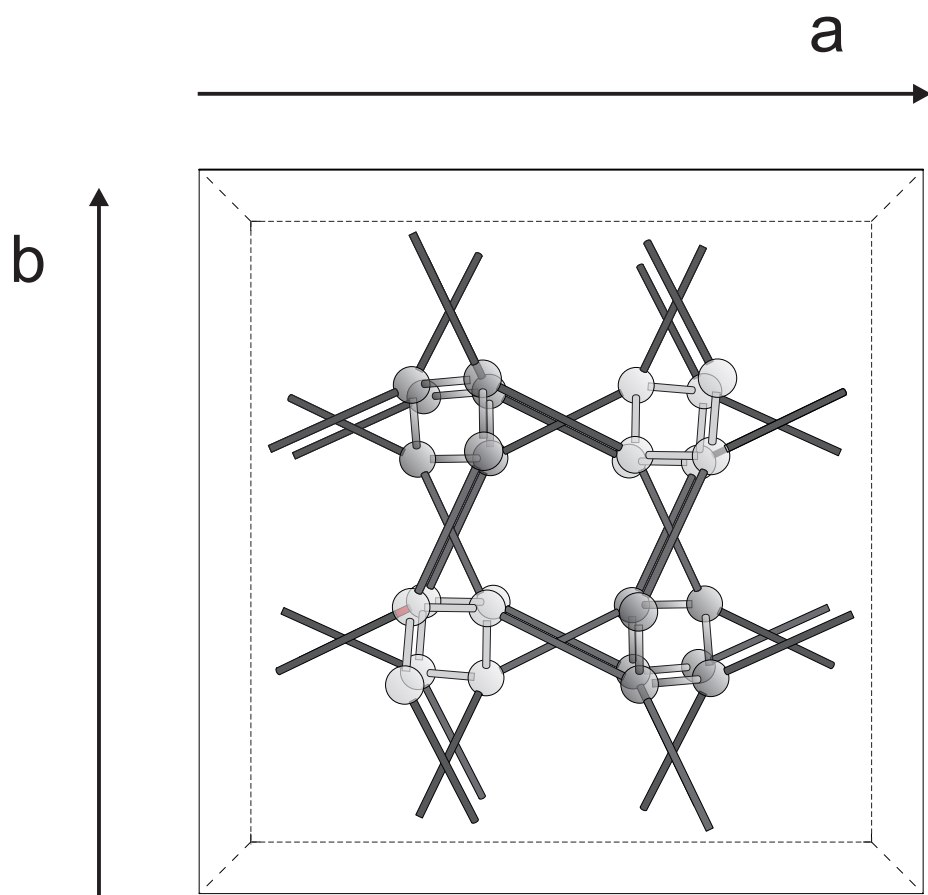
FIG. 14. Measured temperature dependence of the 3D gap energies in for  $\text{SrNi}_2\text{V}_2\text{O}_8$ . The solid lines are as in Fig. 13.

FIG. 15. Relation between the actual structure in  $\text{PbNi}_2\text{V}_2\text{O}_8$  (b) and the equivalent Bravais lattice of spins (a). The notation is as in Appendix II.

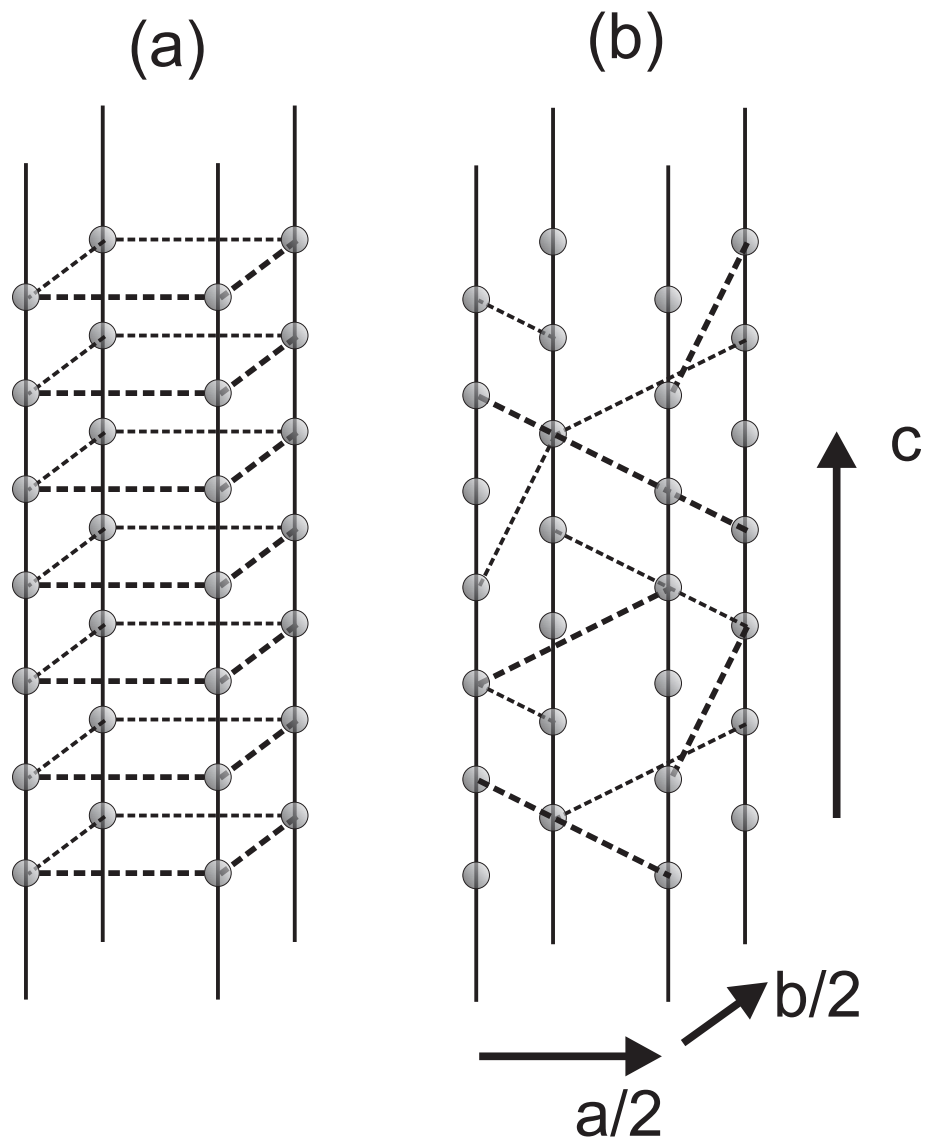


This figure "fig2.jpeg" is available in "jpeg" format from:

<http://arXiv.org/ps/cond-mat/0001374v2>

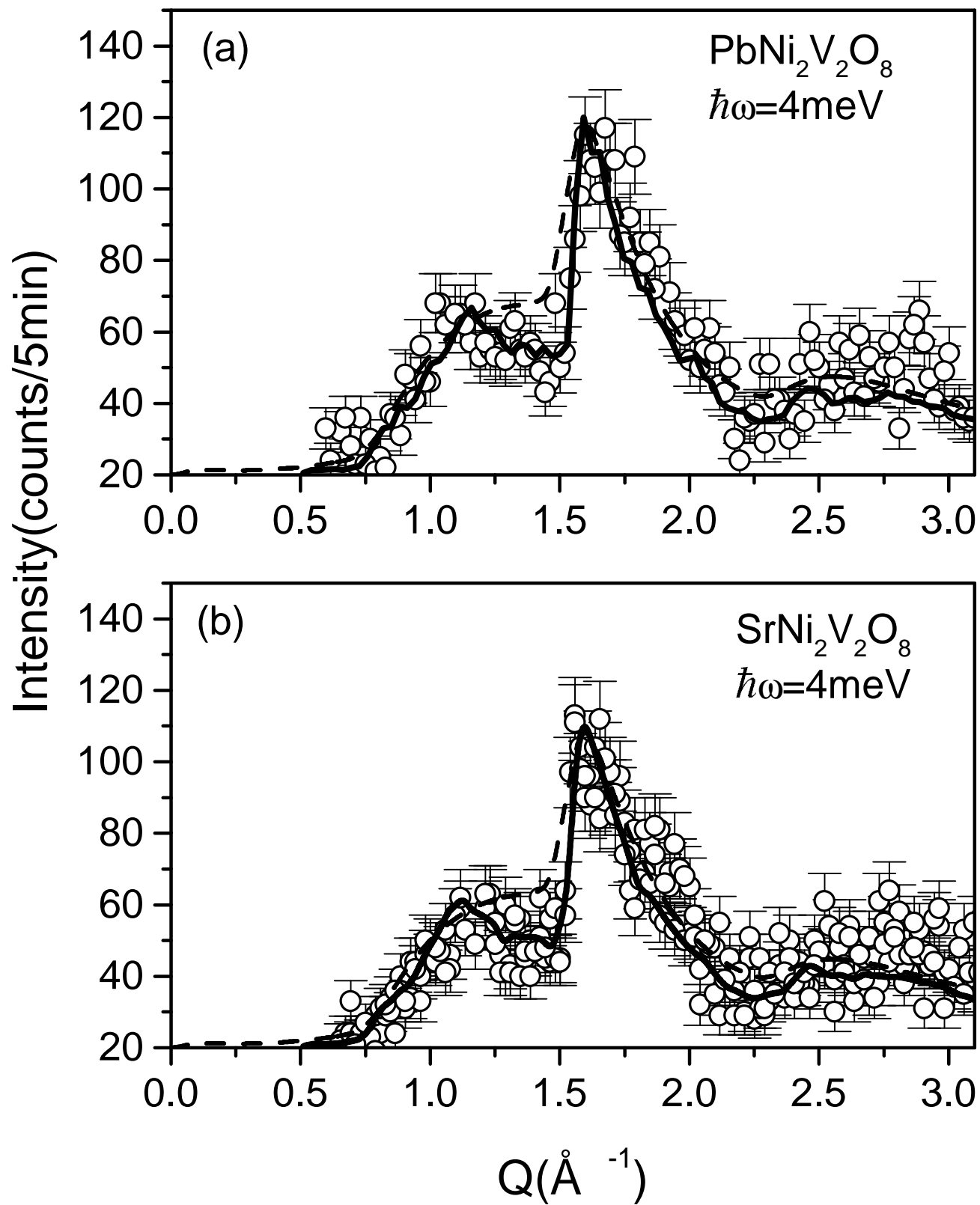


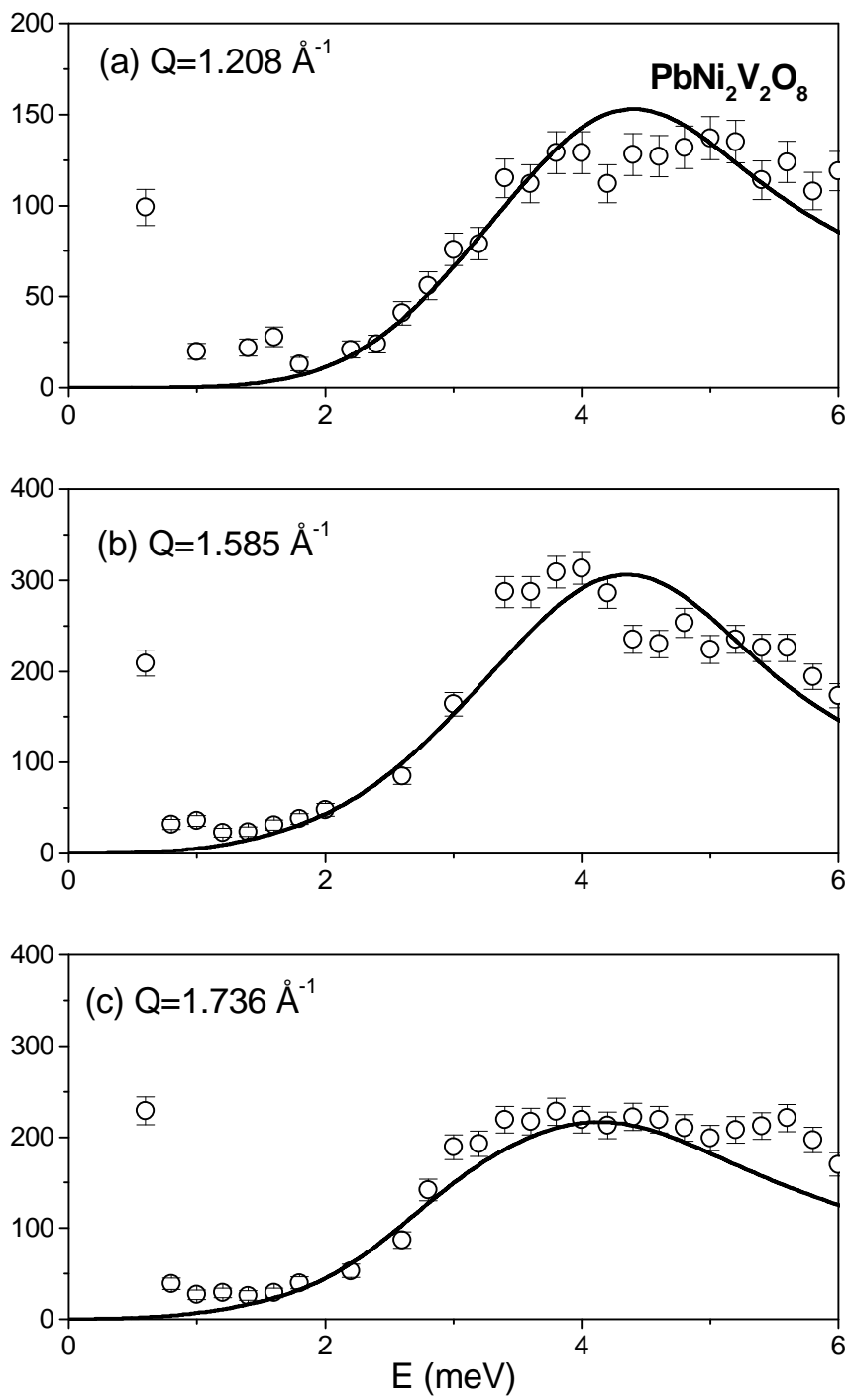


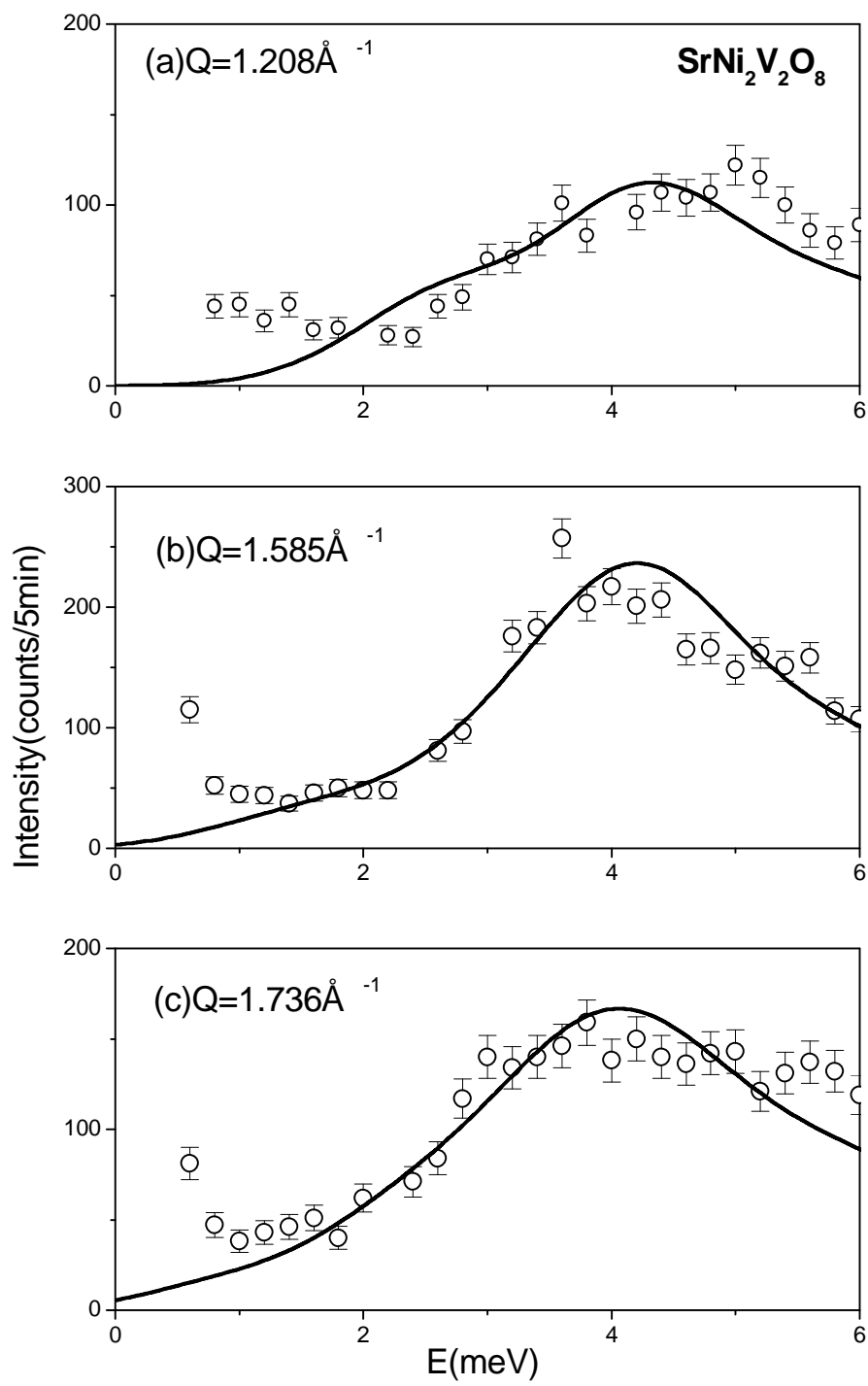


This figure "fig5.jpeg" is available in "jpeg" format from:

<http://arXiv.org/ps/cond-mat/0001374v2>





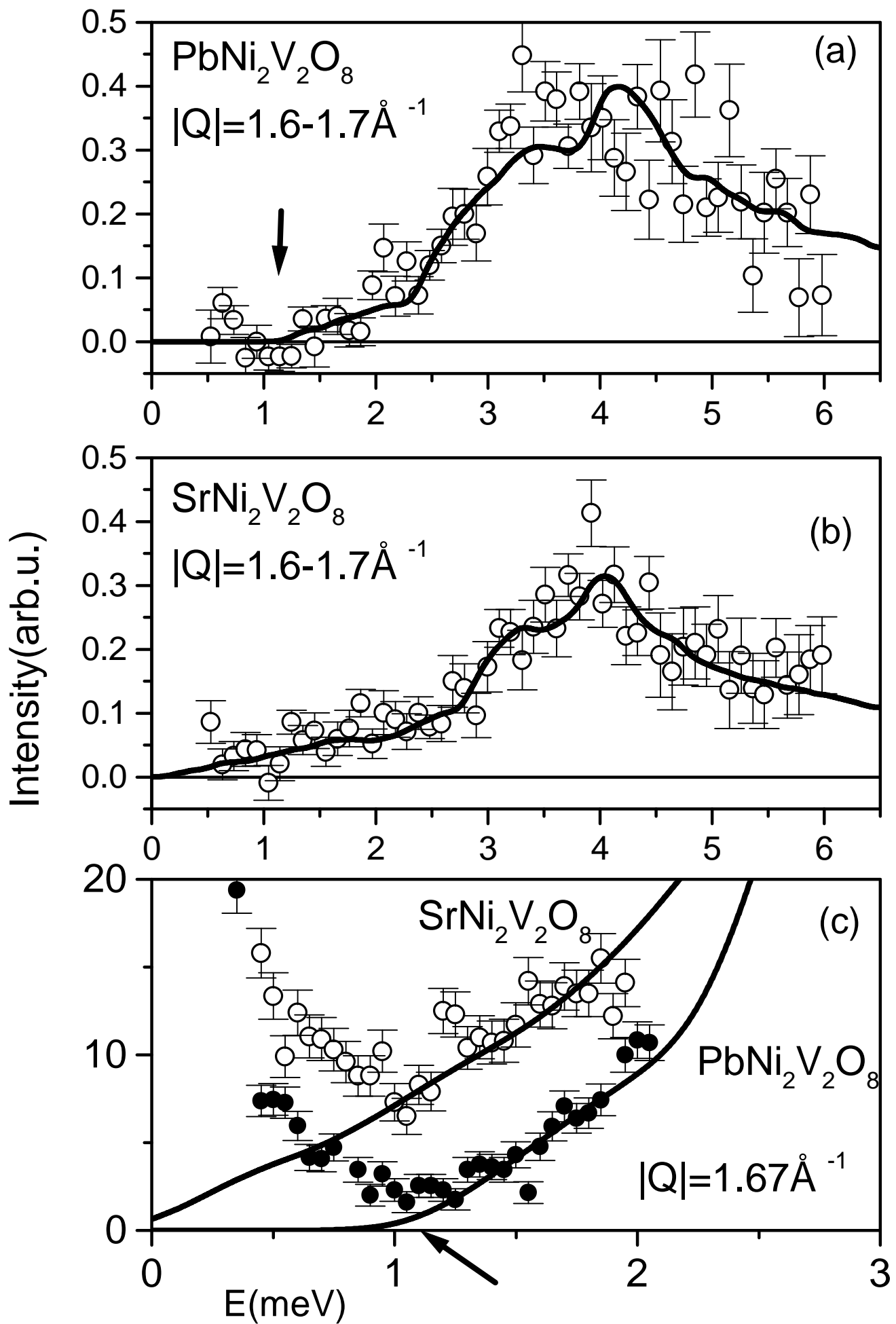


This figure "fig9.jpeg" is available in "jpeg" format from:

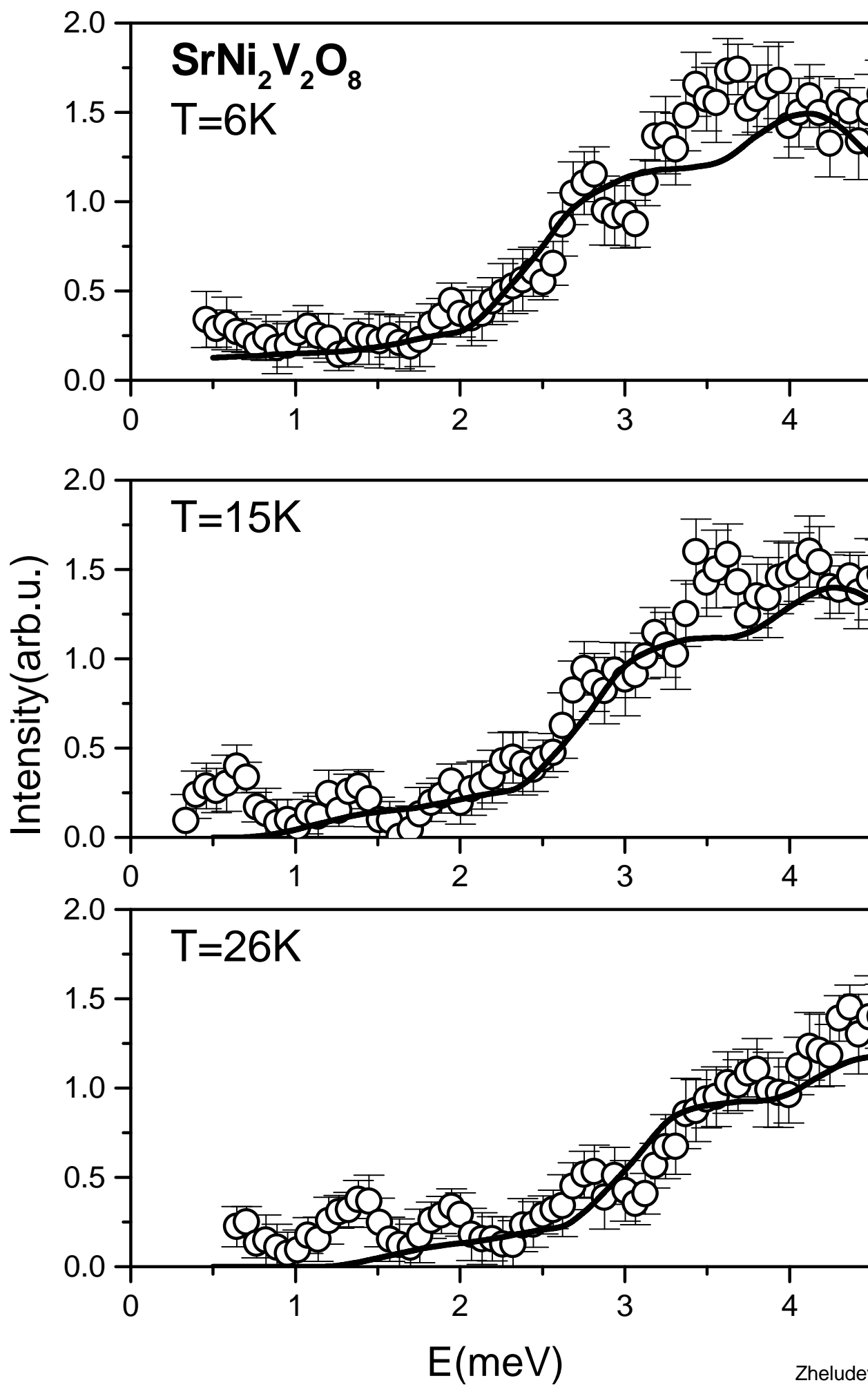
<http://arXiv.org/ps/cond-mat/0001374v2>

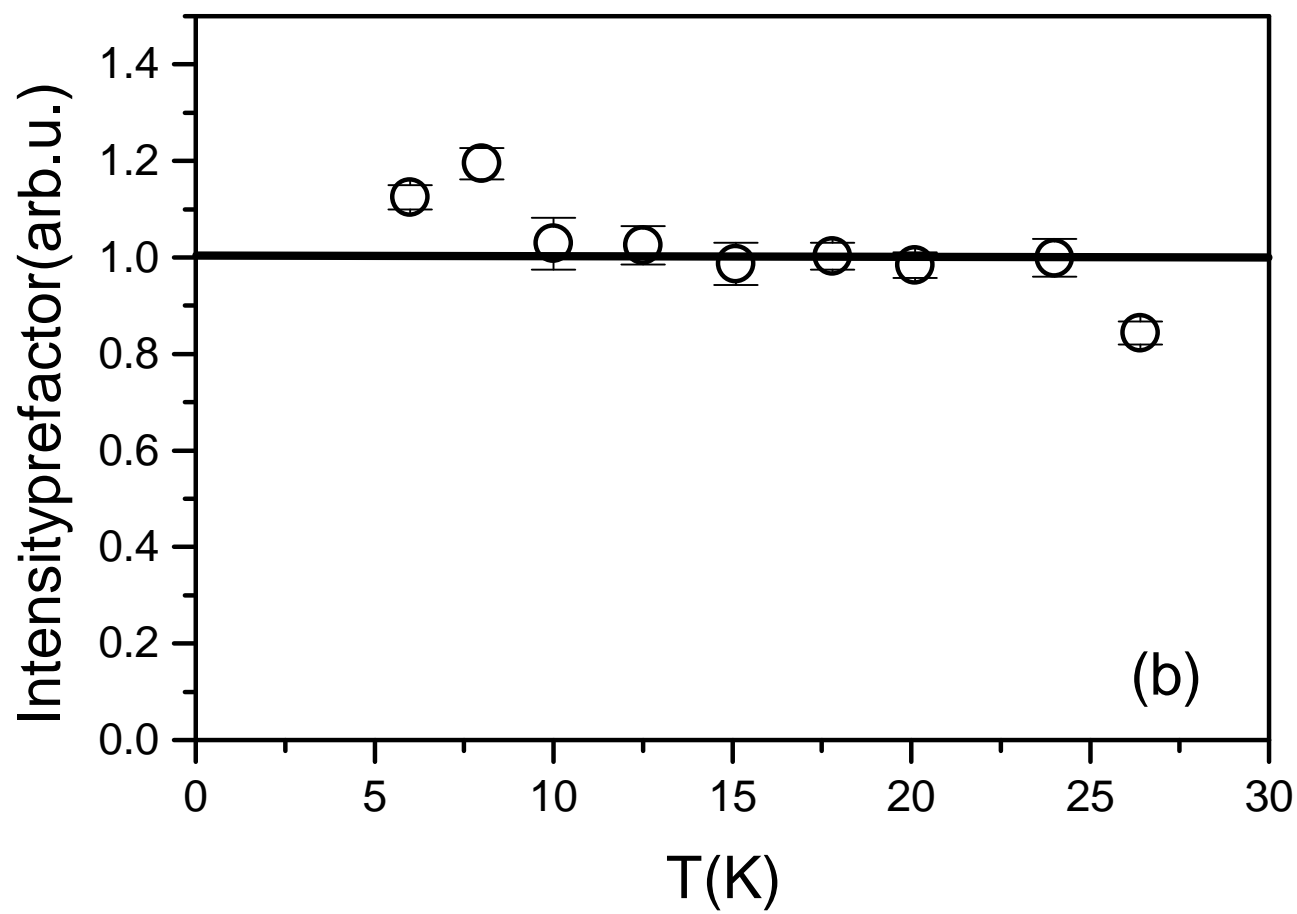
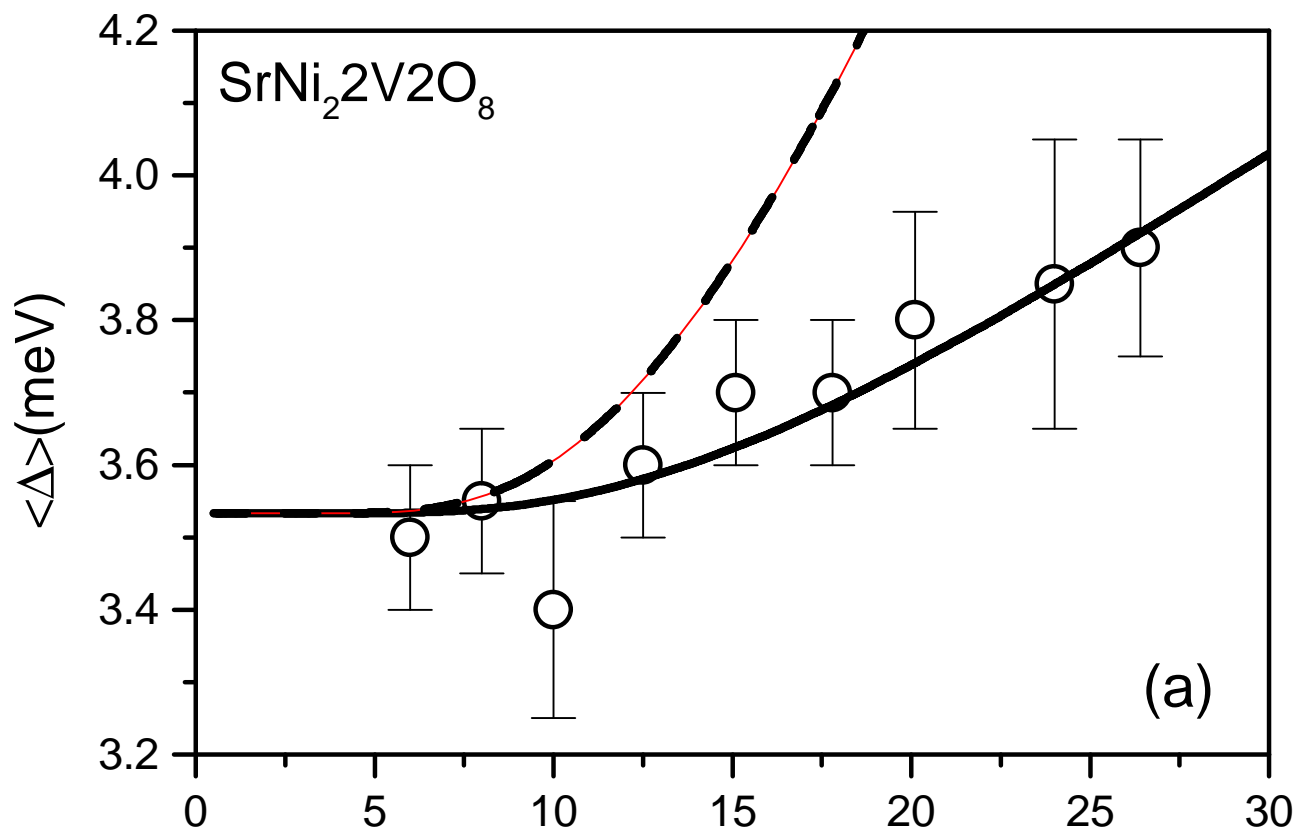
This figure "fig10.jpeg" is available in "jpeg" format from:

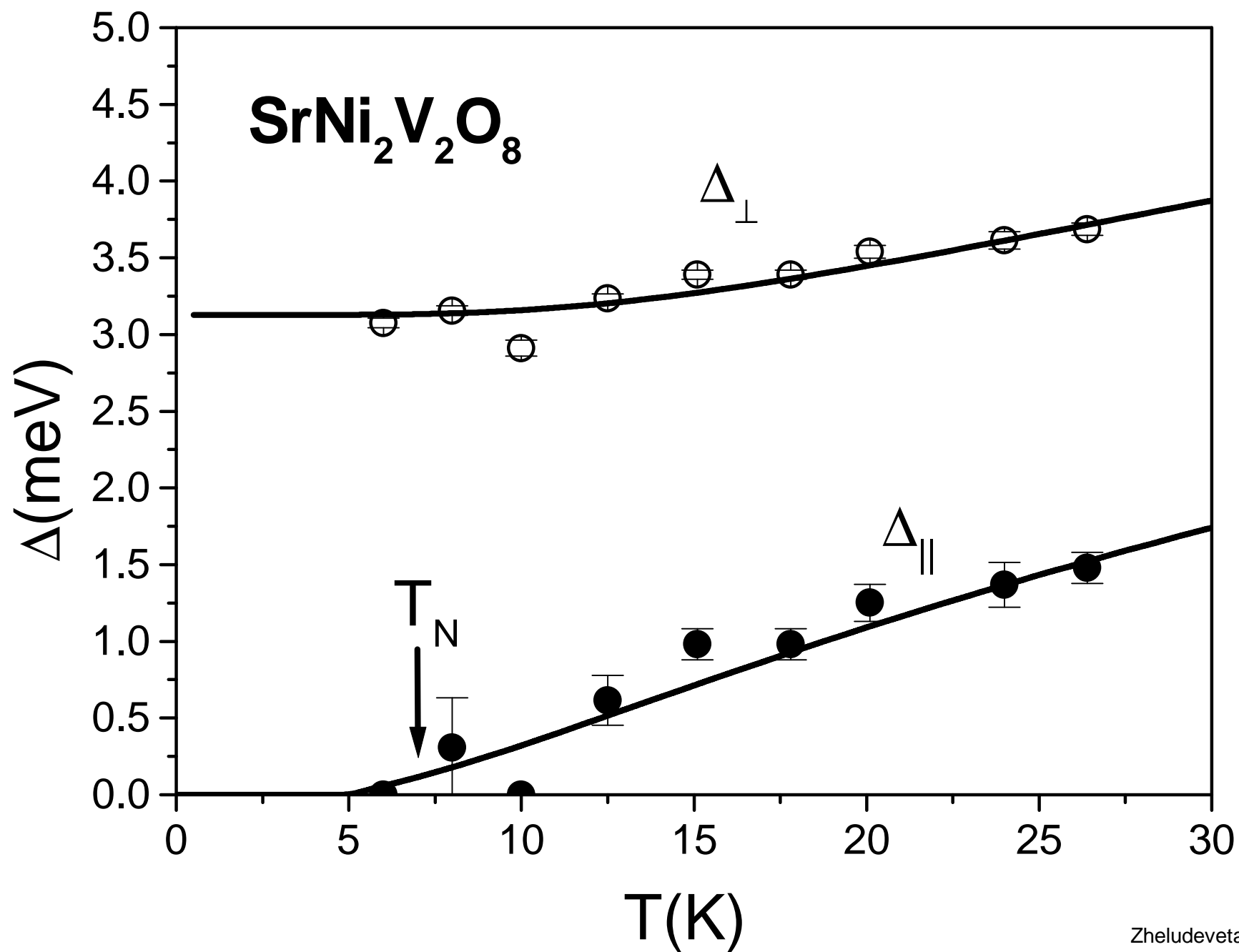
<http://arXiv.org/ps/cond-mat/0001374v2>











This figure "fig15.jpeg" is available in "jpeg" format from:

<http://arXiv.org/ps/cond-mat/0001374v2>